

1 **Correcting Aerosol Extinction Coefficient Vertical Structure Biases in GEOS-**
2 **Chem via a Physics-Informed Transformer with Physical Mechanism Diagnosis**

3 Jiajun Xiong¹, Yi Wang¹, Jun Wang^{2,3}, Yanyu Wang⁴, Meng Zhou^{5,6}, Minghui Tao¹,
4 Wenhui Dong¹, Jhoon Kim⁷, Lunche Wang¹

5 ¹Hubei Key Laboratory of Regional Ecology and Environmental Change, School of
6 Geography and Information Engineering, China University of Geosciences, Wuhan,
7 430074, China

8 ²Department of Chemical and Biochemical Engineering, The University of Iowa, Iowa
9 City, IA 52242, USA

10 ³Center for Global and Regional Environmental Research, The University of Iowa,
11 Iowa City, IA 52242, USA

12 ⁴State Environmental Protection Key Laboratory of Formation and Prevention of Urban
13 Air Pollution Complex, Shanghai Academy of Environmental Sciences, Shanghai
14 200233, China

15 ⁵Goddard Earth Sciences Technology and Research, University of Maryland, Baltimore
16 County, MA 21250, USA

17 ⁶NASA/Goddard Space Flight Center, Global Modeling and Assimilation Office,
18 Greenbelt, MD 20771, USA

19 ⁷Department of Atmospheric Sciences, Yonsei University, Seoul, 03722, South Korea

20 *Correspondence to:* Yi Wang (wangyi34@cug.edu.cn)

Abstract

21

22

23

24

25

26

27

28

29

30

31

32

33

34

35

36

37

38

39

40

41

42

43

44

45

46

47

48

Accurately characterizing aerosol vertical distributions is essential for evaluating radiative forcing and air quality. While Chemical Transport Models (CTMs) simulate spatially continuous Aerosol Extinction Coefficient (AEC, km^{-1}), they exhibit systematic AEC biases. Cloud-Aerosol Lidar with Orthogonal Polarization (CALIOP) observations provide precise AEC profiles but are constrained by sparse spatial sampling. To bridge this gap, we propose a physics-informed Transformer framework as a supervised bias-correction model to correct biases in the AEC profiles simulated by GEOS-Chem. Unlike a standard Transformer, our framework features a dual-stream architecture with explicit physical constraints. It employs gated feature fusion to integrate vertical structures (combining GEOS-Chem priors with MERRA-2 profiles) by dynamically identifying height-dependent drivers, and leverages cross-attention to incorporate MERRA-2 surface environmental constraints for modulating AEC vertical rectification with synoptic contexts. This approach effectively predicts systematic biases relative to CALIOP satellite observations and resolves AEC profiles, surpassing methods retrieving only aerosol layer heights. Leave-One-Year-Out validation over East Asia during 2017–2019 demonstrates significant AEC precision improvements, increasing R from 0.49–0.53 in the GEOS-Chem simulations to 0.66–0.73 and reducing RMSE by approximately 25%. The model effectively mitigates over-diffusion, significantly reducing AEC simulation biases in the critical near-surface layer while capturing smoothed biomass burning and dust plumes. Additionally, it exhibits robust cross-continental transferability, reproducing bias patterns over the North American domain ($R=0.70$) without retraining, confirming the internalization of universal physicochemical relationships linking atmospheric states to simulation biases. Furthermore, interpretability analysis serves as a diagnostic tool to guide physical model improvement. The model identifies temperature and sensible heat flux as primary drivers to constrain boundary layer mixing, pointing to potential uncertainties in vertical eddy diffusion. Additionally, it uses environmental proxies (e.g., vegetation

49 indices and diffuse radiation) to diagnose potential deficiencies in dust threshold
50 friction velocity and secondary organic aerosol yields. These insights provide a physical
51 basis for refining parameterization schemes in CTMs.

52 **Keywords:** Aerosol extinction coefficient profiles, Deep learning, Chemical transport
53 models, CALIOP, Model interpretability

54 **1. Introduction**

55 Atmospheric aerosols are key modulators of the Earth's climate radiative forcing
56 (Kahn et al., 2005; Stier et al., 2007; Dong et al., 2023; Wang et al., 2023) and
57 environmental health (Chen et al., 2022b; Song et al., 2025). As Aerosol Optical Depth
58 (AOD) serves as a fundamental column-integrated parameter (Kaufman et al., 2002), it
59 fails to reveal critical vertical distribution information (Winker et al., 2010; Lu et al.,
60 2025b; Zhu et al., 2024). In reality, the vertical structure of aerosols—characterized by
61 Aerosol Extinction Coefficient (AEC) profiles (Xiong et al., 2026; Jiang et al., 2024;
62 Zhen et al., 2024) and layer heights (Wang et al., 2013; Kim et al., 2025; Yorks et al.,
63 2023; Fan et al., 2025)—is the core physical quantity determining their climatic and
64 environmental effects. Specifically, the vertical distribution governs the atmospheric
65 radiative energy budget and thermal structure; the altitude of absorbing aerosols
66 determines heating rate profile (Lu et al., 2020; Xu et al., 2016) and atmospheric
67 stability (Koch and Del Genio, 2010), and failure to resolve this vertical feature leads
68 to significant radiative forcing estimate biases (Zarzycki and Bond, 2010; Myhre et al.,
69 2013; Shi et al., 2021; Wang et al., 2014). Second, the vertical co-existence of aerosols
70 and clouds is a prerequisite for aerosol-cloud interactions (Zarzycki and Bond, 2010;
71 Ge et al., 2014), meaning that relying solely on column totals hinders the accurate
72 quantification of aerosol impacts on cloud microphysics (Lu et al., 2025b; Wilcox, 2012;
73 Christensen et al., 2020; Zhao et al., 2019). Finally, vertical stratification bridges
74 regional pollution with global transport: aerosols uplifted into the free troposphere
75 undergo intercontinental transport (Val Martin et al., 2013; Weinzierl et al., 2017; Choi
76 et al., 2024), whereas those trapped within the Planetary Boundary Layer (PBL) directly
77 determine surface PM_{2.5} concentrations (Chen et al., 2022a; Handschuh et al., 2022)
78 and health outcomes (Diner et al., 2018). Therefore, precisely characterizing AEC
79 profiles is not only a vital supplement to traditional AOD analysis (Lv et al., 2016; Wei
80 et al., 2019) but also a cornerstone for reducing climate model uncertainties and
81 understanding transboundary pollutant transport.

82 Despite the recognized importance of aerosol vertical distribution, acquiring high-
83 precision, spatiotemporally continuous, and vertically resolved three-dimensional (3D)
84 aerosol information globally remains a formidable challenge. Current characterization
85 methods primarily follow two pathways: passive remote sensing retrieval and active
86 remote sensing observation. With extensive swath widths, passive satellite sensors,
87 such as the TROPOspheric Monitoring Instrument (TROPOMI) and Himawari-8, have
88 made strides in retrieving Aerosol Layer Height (ALH) (Lu et al., 2025a; Nanda et al.,
89 2020). Utilizing differential absorption in oxygen bands (O_2 A/B) (Ding et al., 2016;
90 Nanda et al., 2018; Chen et al., 2025; Sanders et al., 2015) or multi-angle stereoscopic
91 techniques (Kahn et al., 2005; Dubovik et al., 2011), these algorithms estimate the
92 effective ALH. However, the effective ALH merely represents the optical centroid or a
93 vertically weighted average of the aerosol column, rather than a resolved vertical profile
94 (Chimot et al., 2018; Lu et al., 2025b). While valuable for tracking plumes (Huang et
95 al., 2024), it fails to resolve complex multilayer structures (Winker et al., 2013) and
96 cannot provide the vertical gradients of AEC necessary for calculating radiative heating
97 rates (Samset et al., 2013). In contrast, spaceborne active lidars—specifically the
98 Cloud-Aerosol Lidar with Orthogonal Polarization (CALIOP)—offer high-resolution
99 Aerosol Extinction Profiles (AEPs) that resolve aerosol stratification (Liu et al., 2012;
100 Huang et al., 2013; Wang et al., 2021a). Nevertheless, constrained by narrow nadir-
101 viewing geometry (Winker et al., 2009; Hunt et al., 2009) and sparse sampling, active
102 remote sensing suffers from substantial observational gaps, producing a "curtain-like"
103 dataset rather than planar coverage (Koffi et al., 2012b; Colarco et al., 2014). To bridge
104 these gaps, Chemical Transport Models (CTMs, e.g., GEOS-Chem and WRF-Chem)
105 are indispensable for simulating continuous 3D aerosol fields (Xiong et al., 2026; Jiang
106 et al., 2024). However, these models are often hampered by uncertainties in emission
107 inventories (Bond et al., 2013; Hoesly et al., 2018; Liang et al., 2023) and simplified
108 physical parameterizations (e.g., wet scavenging, boundary layer turbulent mixing)
109 (Xiong et al., 2026; Du et al., 2020; Zeng et al., 2020), leading to systematic biases and

110 misalignment with lidar observations (Koffi et al., 2016; Koffi et al., 2012a; Kim et al.,
111 2015).

112 To bridge the gap between sparse observations and biased simulations, traditional
113 studies have employed Data Assimilation (DA) techniques, such as 3D-Var or Kalman
114 Filtering (Henze et al., 2009; Sekiyama et al., 2010; Wang et al., 2020b; Henze et al.,
115 2007; Wang et al., 2020a; Zhang et al., 2011). However, operational DA schemes often
116 face prohibitive computational costs (Benedetti et al., 2018) and rely on Gaussian error
117 assumptions that may not match the complex, non-linear characteristics of aerosol
118 processes (Bocquet et al., 2010; Geer, 2021). Driven by the exponential growth of
119 atmospheric big data, Deep Learning (DL) has emerged as a transformative alternative
120 for bias correction and multi-source data fusion (Geer, 2021; Wang et al., 2022; Xing
121 et al., 2022; Fan et al., 2025). Early studies successfully applied Random Forests or
122 Deep Neural Networks to improve AOD retrieval (Sanders et al., 2015) or surface PM_{2.5}
123 estimation (Hu et al., 2014; Wei et al., 2019; Li et al., 2017). More recently,
124 Convolutional Neural Networks (CNNs) have been utilized to estimate AEPs by
125 extracting spatial texture features from passive satellite imagery (Zhen et al., 2024).
126 However, these methods typically simplify profile estimation into a point-wise
127 regression problem (Pashayi et al., 2025; Li et al., 2020; Yang et al., 2025) or rely
128 heavily on two-dimensional (2D) spatial convolutions (Daoud et al., 2021).
129 Consequently, they often neglect the inherent sequential correlation and physical
130 coupling of the aerosol vertical structure. In reality, the aerosol state at a specific altitude
131 is intimately linked to layers above and below through turbulent mixing and
132 sedimentation (Zeng et al., 2020; Xiong et al., 2026; Du et al., 2020). Standard CNNs
133 or pixel-wise models struggle to capture this long-range dependency along the vertical
134 axis (Wang et al., 2021b) and often overlook the structural priors provided by CTMs
135 (Reichstein et al., 2019; Geer, 2021). To overcome these limitations, the Transformer
136 architecture (Vaswani et al., 2017), originally designed for sequence modeling, offers a
137 superior solution. Its self-attention mechanism dynamically weighs information from

138 different altitude layers, effectively capturing global vertical dependencies within the
139 atmospheric column. This capability makes it an effective tool for fusing the physical
140 consistency of GEOS-Chem simulations with the vertical precision of CALIOP
141 observations to derive high-precision 3D AEC fields.

142 To address the spatiotemporal sparsity of spaceborne lidar observations and the
143 inherent simulation biases of CTMs, this study proposes a physics-informed
144 Transformer DL framework aimed at correcting systematic biases to yield high-
145 precision, spatially continuous 3D AEC fields. Distinct from traditional DA systems
146 that require concurrent observational inputs to iteratively update state variables, our
147 framework operates as a supervised bias-correction model. It captures the intrinsic
148 state-dependent mapping between CTM structural uncertainties and diverse
149 environmental contexts. By conditioning the correction exclusively on the CTM's a
150 priori state and meteorological drivers, the model effectively mitigates systematic
151 biases without relying on CALIOP data during the inference phase. Furthermore,
152 distinct from data-driven retrieval methods that rely solely on passive remote sensing
153 imagery, our approach explicitly embeds the vertical structural priors provided by
154 GEOS-Chem simulations and meteorological constraints from Modern-Era
155 Retrospective analysis for Research and Applications, Version 2 (MERRA-2) reanalysis
156 data. Leveraging the self-attention mechanism unique to the Transformer architecture,
157 the model effectively captures and corrects the complex, non-linear bias patterns
158 between simulated results and CALIOP observational benchmarks. Focusing on East
159 Asia (EA) from 2017 to 2019, we systematically evaluate the framework's performance
160 in bias correction and spatiotemporal generalization. Crucially, to overcome the black-
161 box limitations of DL, we integrate SHapley Additive exPlanations (SHAP) (Lundberg
162 and Lee, 2017) with attention weight analysis to quantitatively parse the contributions
163 of meteorological factors and aerosol variables to the bias correction process. This
164 process not only enables an interpretable diagnosis of CTM simulation biases—
165 identifying the dominant drivers of bias within specific altitudes or regions—but also

166 bridges data-driven correction with the targeted refinement of GEOS-Chem’s physical
167 parameterizations. The remainder of this paper is organized as follows. Section 2
168 introduces the multi-source datasets and model configurations. Section 3 details the
169 physics-informed Transformer architecture and evaluation strategies. Section 4
170 evaluates the bias correction performance against observations and elucidates the
171 physical drivers of simulation biases through interpretability analysis. Finally, Section
172 5 summarizes the conclusions.

173

174 **2. Data and Model Configuration**

175 **2.1 Study Region**

176 This study focuses primarily on EA (0° - 60° N, 70° - 150° E, Fig. 1), a domain
177 characterized by complex aerosol sources and intense aerosol-meteorology interactions,
178 serving as the core region for training and evaluating the bias-correction model. Within
179 the EA domain, six Regions of Interest (ROI) are selected to evaluate performance
180 across distinct aerosol regimes (Fig. 1): the anthropogenic-dominated North China
181 Plain (NCP) and Indo-Gangetic Plain (IGP), the dust-active Taklamakan Desert, the
182 smoke-impacted Indochina Peninsula, and the cleaner Tibetan Plateau and Western
183 Pacific. To investigate vertical characteristics in the lower troposphere extending from
184 the surface to 6 km Above Ground Level (AGL), we establish three spatial diagnostics:
185 a 38° N transect (70° - 150° E) capturing the zonal source-to-sink continuum driven by
186 the Westerlies; a 40° N transect (120° - 150° E) targeting the dispersion of continental
187 outflow over marine surfaces; and a domain-wide zonal mean profile (0° - 60° N) to
188 reveal the macroscopic latitudinal dependence of aerosol loading and layer heights. To
189 rigorously assess the model’s spatial generalization capability, we additionally define
190 an independent validation sub-region over North America (NA, 25° - 55° N, 70° - 130° W).

191 **2.2 CALIOP**

192 The CALIOP sensor onboard the Cloud-Aerosol Lidar and Infrared Pathfinder
193 Satellite Observations (CALIPSO) satellite serves as the observational benchmark for

194 characterizing aerosol vertical structure and quantifying simulation biases. We utilize
195 the Level 2 Version 4.51 Aerosol Profile product, which provides vertical profiles of
196 AEC at 532 nm and 1064 nm. The standard Level 2 product offers a uniform horizontal
197 resolution of 5 km and a vertical resolution of 60 m throughout the troposphere (–0.5
198 km to 20 km). Given that aerosol loading is predominantly confined to the PBL and
199 lower free troposphere (Xiong et al., 2026; Jiang et al., 2024), our analysis is restricted
200 to the altitude range of 0–6 km AGL.

201 To ensure data reliability, we implement a rigorous, tiered Quality Control (QC)
202 procedure to exclude profiles contaminated by clouds or compromised by retrieval
203 artifacts (detailed in Sect. S1). This stringent assessment framework substantially
204 enhances the precision of the CALIOP dataset for model training (Hong and Di
205 Girolamo, 2022; Jiang et al., 2024; Xiong et al., 2026; Mehta et al., 2023; Winker et al.,
206 2013).

207 To ensure physical consistency between the GEOS-Chem and CALIOP satellite
208 observations, we employ a strict spatiotemporal collocation strategy. Spatially, the high-
209 resolution CALIOP Level 2 profiles are mapped onto the GEOS-Chem grid. All quality-
210 controlled CALIOP profiles falling within a specific grid cell are spatially averaged to
211 represent the observational mean state of that grid box. Temporally, we adopt a precise
212 nearest-hour collocation approach. The CALIOP overpass times are mathematically
213 rounded to the nearest UTC hour and paired strictly with the GEOS-Chem 1-hourly
214 instantaneous outputs. Aligning the instantaneous model output with the concurrent
215 instantaneous observation minimizes temporal representativeness errors (typically
216 constrained within ± 30 minutes) (Ichoku et al., 2002). However, we acknowledge that
217 this approach inherently introduces spatial representativeness errors. Averaging the
218 narrow, "curtain-like" nadir view of CALIOP to represent a bulk $2^\circ \times 2.5^\circ$ grid box
219 inevitably suffers from sub-grid heterogeneity, particularly in regions with complex
220 terrain or localized intense emissions.

221 In our physics-informed data-driven framework, the collocated CALIOP AEPs are

222 treated as the observational benchmarks. The training target for the Transformer model
223 is explicitly defined as the simulation bias, calculated as the deviation of the GEOS-
224 Chem simulated AEC from the corresponding CALIOP observations (detailed in Sect.
225 3.1). However, it is essential to acknowledge the intrinsic uncertainties associated with
226 satellite retrievals. Validations against ground-based AERONET measurements
227 indicate a mean relative bias in CALIOP AOD of approximately $-5.1\% \pm 8.5\%$ (Kim et
228 al., 2018). Furthermore, the agreement between CALIOP 532 nm calibrated attenuated
229 backscatter and airborne High Spectral Resolution Lidar (HSRL) measurements is
230 typically within $1.0\% \pm 3.5\%$ (Getzewich et al., 2018). These inherent observational
231 uncertainties, coupled with the spatial representativeness errors, impose a theoretical
232 upper limit on the precision of the bias correction method proposed herein.

233 **2.3 AERONET**

234 To independently evaluate the model's capability in capturing high-frequency
235 temporal variations—bridging the observational gaps inherent to the sparse sampling
236 of polar-orbiting satellites—we utilize AOD data from the AERONET (Holben et al.,
237 1998). Specifically, the Version 3 Level 2.0 (cloud-screened and quality-assured) AOD
238 data are employed (Giles et al., 2019). Since AERONET instruments do not directly
239 measure AOD at 532 nm, data are interpolated to this wavelength using the Ångström
240 exponent derived from adjacent channels (detail in Sect. S2). Two representative sites
241 are selected for detailed case studies, targeting distinct aerosol regimes during high-
242 loading episodes (Fig. 1). (1) Kanpur (26.5°N , 80.2°E): Located in the IGP, this site is
243 characterized by a complex mixture of anthropogenic pollution and transported dust.
244 We focus on a 7-day window centered on 30 April 2019, representing a typical pre-
245 monsoon scenario driven by regional dust and haze activity (Misra et al., 2014; Singh
246 et al., 2004; Chinnam et al., 2006); (2) Nong Khai (17.9°N , 102.7°E): Situated in the
247 Indochina Peninsula, this site is dominated by carbonaceous aerosols resulting from
248 intense agricultural biomass burning (Munroe et al., 2008; Nguyen et al., 2021). The
249 analysis window is centered on 22 February 2019, coinciding with the peak of the

250 regional active fire season (Tsay et al., 2013). Examining these high-loading cases
251 allows us to assess the robustness of the model in reproducing the dynamic evolution
252 of pollution accumulation and dissipation, providing a rigorous test of the temporal
253 consistency of our bias correction approach.

254 **2.4 GEOS-Chem and Meteorological Reanalysis**

255 We employ the GEOS-Chem (Bey et al., 2001) global CTM (version 13.4.0) to
256 simulate the 3D distribution of atmospheric composition, focusing on the EA domain
257 defined in Section 2.1. The simulation spans from 1 January 2017 to 31 December 2019.
258 The model is driven by the MERRA-2 assimilated meteorological fields provided by
259 the NASA Global Modeling and Assimilation Office (GMAO) (Gelaro et al., 2017). To
260 accommodate the spatially sparse sampling inherent to CALIOP's nadir-viewing
261 geometry, the simulation is configured at a horizontal resolution of $2^\circ \times 2.5^\circ$ (latitude
262 \times longitude) with 47 vertical hybrid sigma-pressure levels extending from the surface
263 to 0.01 hPa. Anthropogenic emissions are prescribed by the Community Emissions
264 Data System (CEDSV2) (McDuffie et al., 2020). Biogenic emissions of Volatile Organic
265 Compounds (BVOCs) are prescribed using the offline MEGAN inventory (Guenther et
266 al., 2012). Biomass burning emissions are derived from the Global Fire Emissions
267 Database version 4 (GFED4) (Giglio et al., 2013). GEOS-Chem is operated in the
268 "Standard Full Chemistry" mode, utilizing a fully coupled NO_x - O_x -hydrocarbon-
269 aerosol mechanism. The aerosol simulation encompasses sulfate, nitrate, ammonium,
270 carbonaceous aerosols, mineral dust, and sea salt. Both dry and wet deposition
271 processes are explicitly treated to characterize aerosol sinks. Vertical transport is
272 parameterized using a non-local PBL mixing scheme, which accounts for deep
273 convective updrafts and turbulent diffusion (Lin and McElroy, 2010). To facilitate direct
274 comparison with CALIOP observations, the model is configured to diagnose and
275 archive 3D AEC directly at 532 nm with a 1-hour temporal resolution.

276 MERRA-2 reanalysis data serve a dual purpose in this study: acting as the driving
277 meteorological field for the GEOS-Chem and constituting the key physical input

278 features for the physics-informed Transformer model. Integrating these meteorological
279 state variables into the DL framework aims to explicitly capture the non-linear
280 dependence of simulation biases on synoptic and micro-meteorological conditions.
281 Generated by the GEOS-5 atmospheric general circulation model combined with 3D
282 variational DA, MERRA-2 provides globally consistent physical fields. To maintain
283 consistency within our physics-informed data-driven framework, we extract
284 meteorological variables that are strictly consistent with those driving GEOS-Chem.
285 These variables are regridded to the $2^\circ \times 2.5^\circ$ resolution to achieve strict spatial
286 alignment with the aerosol simulation outputs, jointly constructing the "meteorological
287 background" vector in the neural network's input layer.

288

289 **3. Method**

290 **3.1 Input Feature Construction and Target Definition**

291 We design a dual-stream input architecture to decouple local vertical atmospheric
292 states from synoptic meteorological forcing. The detailed inventory of all input
293 variables is provided in Section S3 in the supplement.

294 The Vertical Profile Stream (VPS) resolves the atmospheric column through three
295 sub-components. (1) Physicochemical profiles: This includes GEOS-Chem simulated
296 aerosol species and MERRA-2 meteorological profiles. Beyond basic mass
297 concentrations, we explicitly incorporate precursor gases (SO_2 , NO_x , NH_3) and
298 microphysical variables (e.g., hygroscopic growth factors and effective radii) to
299 physically constrain secondary aerosol formation and optical extinction. (2) Height
300 information: To maintain vertical stratification within the attention mechanism, we
301 embed explicit altitude information. This allows the model to correctly differentiate
302 near-surface emission interactions from free-tropospheric long-range transport. (3)
303 Spatiotemporal indices: Geographical coordinates (latitude, longitude) and temporal
304 indices (month, day, night) are projected into high-dimensional vectors to capture
305 regional emission patterns and seasonal cycles.

306 The Synoptic Forcing Stream (SFS) incorporates 2D surface diagnostics to
307 represent synoptic constraints on the atmospheric column. Variables such as Planetary
308 Boundary Layer Height (PBLH) and friction velocity act as indicators for turbulent
309 mixing. Surface fluxes and Leaf Area Index (LAI) parameterize deposition and
310 biogenic emissions, while precipitation rates serve as proxies for wet scavenging.

311 Furthermore, although our architecture does not employ explicit historical time-
312 series modeling, it robustly captures diurnal variability. By rigorously matching the
313 instantaneous MERRA-2 fields with the exact CALIOP overpass time, the model is
314 directly conditioned on the concurrent thermodynamic and dynamic states. Combined
315 with explicit day/night flags, this allows the framework to dynamically resolve
316 meteorology-driven diurnal processes (e.g., boundary layer evolution and
317 photochemistry) without relying on lagged predictors.

318 Finally, we define the learning target Δ_{AEC}^{target} as the systematic bias of GEOS-
319 Chem simulated AEC (AEC_{GC}) evaluated against CALIOP observation (AEC_{CAL}):

$$320 \quad \Delta_{AEC}^{target} = AEC_{GC} - AEC_{CAL} \quad (1)$$

321 Predicting the simulation bias Δ_{AEC}^{target} , rather than the absolute AEC magnitude,
322 ensures the framework preserves the fundamental physical transport patterns resolved
323 by the CTM, focusing solely on correcting systematic deviations caused by
324 parameterization or emission uncertainties. It is important to emphasize that while
325 CALIOP observations provide the target during training, they are strictly excluded from
326 the input feature space during inference. Consequently, the framework’s corrective
327 capacity is inherently bounded by the information content of the GEOS-Chem and
328 MERRA-2 predictors. The model is designed to rectify state-dependent systematic
329 biases rather than to artificially generate aerosol signals from completely unrepresented
330 physical processes that lack corresponding perturbation signatures in the input fields.

331 It should be noted that using CALIOP retrievals as the baseline inherently
332 propagates its systematic uncertainties (e.g., a mean relative bias of -5.1%, as discussed

333 in Sect. 2.2) into the learning target. If CALIOP exhibits a systematic negative bias, the
334 model may theoretically learn a tendency to slightly over-compensate the AEC.
335 However, because GEOS-Chem's structural biases are typically an order of magnitude
336 larger than these observational uncertainties, the data-driven correction remains highly
337 beneficial. A detailed quantitative evaluation of the model's sensitivity to these
338 observational uncertainties is presented in Section 4.1.5.

339 **3.2 Physically-Informed Transformer Architecture**

340 The overall architecture of our proposed framework (Figure 2) bridges GEOS-
341 Chem simulations and CALIOP observations. To preserve the distinct structural
342 characteristics of atmospheric profiles and synoptic environmental contexts, the
343 framework processes these two streams through specialized embedding strategies
344 (detailed in Sect. S4a, b). The model comprises an altitude-dependent gated feature
345 fusion mechanism, a Transformer encoder for vertical dependencies, a cross-attention
346 module for synoptic constraints, and an output layer.

347 **3.2.1 Altitude-Dependent Gated Feature Fusion**

348 Physical factors governing AEC vary significantly with altitude. Local emissions
349 and chemical composition dominate near-surface AEC (Xiong et al., 2026; Jiang et al.,
350 2024), whereas long-range transport and regional backgrounds dictate the free
351 troposphere (Uno et al., 2009; Val Martin et al., 2013). To reflect this stratification, we
352 design a gated feature fusion mechanism within the VPS. Instead of statically
353 concatenating inputs, this module dynamically weights the contributions of
354 physicochemical profiles, height information, and spatiotemporal indices for each
355 altitude layer. This allows the model to autonomously prioritize the most relevant
356 physical drivers at specific heights.

357 The SFS incorporates diverse meteorological parameters with distinct physical
358 units. To prevent the network from treating these distinct physical quantities merely as
359 dimensionless numbers, we implement a variable identity embedding (Eq. S4). This
360 mechanism assigns a unique physical tag to each 2D variable, ensuring the model

361 accurately distinguishes between different meteorological forcing factors when
362 modulating the AEC simulation bias.

363 **3.2.2 Modeling Vertical Connectivity and Synoptic Modulation**

364 Aerosol layers are inherently coupled through vertical exchange processes such as
365 turbulent mixing, deep convection, and gravitational sedimentation. We employ a
366 Transformer encoder stack to explicitly model this vertical connectivity. Its self-
367 attention mechanism acts as a dynamic vertical covariance operator (detailed in Sect.
368 S4c). It facilitates information flow between near-surface accumulation layers and high-
369 altitude transport layers, ensuring the rectified AEC profile maintains physical
370 continuity.

371 To constrain this vertical AEC bias correction with synoptic meteorology, we
372 introduce a cross-attention layer. Functionally, this mechanism acts as a dynamic
373 diagnostic process. It allows the aerosol state at each specific altitude to dynamically
374 respond to the prevailing synoptic conditions (e.g., surface wind speed, PBLH), thereby
375 extracting relevant environmental constraints for the local bias adjustment. This design
376 mimics physical reality, where synoptic meteorological backgrounds continuously
377 modulate local microphysical structures.

378 **3.2.3 Output Layer**

379 To predict the final AEC bias, we employ a residual connection that adds the initial
380 baseline state (from the VPS) directly to the output of the cross-attention module (which
381 has already fused the encoded VPS with the SFS). Physically, this residual design serves
382 as a critical prior constraint. It anchors the network to the fundamental atmospheric
383 state provided by GEOS-Chem, ensuring the model computes a meteorology-driven
384 perturbation rather than generating unphysical aerosol signals. Subsequently, the
385 integrated features undergo a progressive dimension-reduction (represented as $D \rightarrow$
386 $D/2 \rightarrow D/4$ in Fig. 2). This architecture functions as an information funnel, filtering
387 redundant meteorological noise and distilling the non-linear interactions among diverse
388 drivers to accurately quantify the true magnitude of the AEC biases.

389 **3.3 Magnitude-Weighted Loss Function**

390 To address the statistical imbalance between the predominant clean background
391 signals and the physically critical pollution episodes, we propose a Magnitude-
392 Weighted Loss (L_{MW} , detailed in Sect. S4g). This customized loss function dynamically
393 rescales the correction weighting to enhance the model's sensitivity to large simulation
394 AEC biases while strictly suppressing spurious aerosol artifacts in atmospheric regimes
395 where the CTM already performs satisfactorily.

396 **3.4 Model Evaluation Strategy**

397 To comprehensively assess the robustness and generalization capability of the
398 physics-informed Transformer model, we design a rigorous evaluation framework
399 covering five dimensions.

400 (1) Spatial block cross-validation: To mitigate information leakage caused by
401 spatial autocorrelation (Geer, 2021), we implement a spatial block K-fold cross-
402 validation strategy (Sect. S5). The study region is divided into non-overlapping $4^\circ \times 5^\circ$
403 blocks (aggregating 2×2 model grids). In each iteration, the model is trained on four
404 folds and evaluated on the remaining spatially independent fold. This "checkerboard"
405 approach ensures performance metrics reflect the model's ability to extrapolate to
406 unseen geographic locations.

407 (2) Temporal transferability: Given the interannual variability in emissions and
408 meteorology (Xiong et al., 2026), we adopt a Leave-One-Year-Out (LOYO) cross-
409 validation scheme comprising three independent experiments (Table 1). This tests
410 whether the model learns generalizable physical rules rather than overfitting to specific
411 temporal patterns.

412 (3) External spatial generalization: To rigorously test the model's transferability
413 beyond its training distribution, we perform an out-of-domain evaluation on the
414 independent NA defined in Section 2.1. By directly applying the model trained on EA
415 data to this unseen continent—which possesses distinct aerosol sources and
416 meteorological backgrounds—we evaluate whether the learned bias-correction

417 mechanism captures universal physical laws rather than region-specific correlations.
418 Furthermore, to dissect the impact of varying aerosol composition regimes on model
419 transferability, the NA validation results are further stratified using CALIOP aerosol
420 subtype classifications.

421 (4) Independent ground-based validation: We employ ground-based AERONET
422 observations as an independent physical benchmark. Predicted AEPs are vertically
423 integrated to derive column AODs, which are then compared with AERONET data to
424 assess the reproduction of high-frequency temporal evolution.

425 (5) Methodological benchmarking: We evaluate the proposed Transformer against
426 conventional machine learning baselines and conduct ablation studies to justify the
427 architectural complexity and isolate the sources of performance improvements.

428 To quantify the model performance across these dimensions, we employ a
429 comprehensive set of statistical metrics, including the Pearson correlation coefficient
430 (R), Mean Absolute Error (MAE), Root Mean Square Error (RMSE), and Normalized
431 Root Mean Square Error (NRMSE). Detailed mathematical definitions are provided in
432 Sect. S6. NRMSE is specifically used to enable fair comparisons across vertical layers
433 by normalizing biases against the exponentially decaying dynamic range of AEC.

434 **3.5 Model Interpretability Framework**

435 To elucidate the inference logic of the correction framework and ensure physical
436 consistency, we establish a hierarchical diagnostic approach. This framework addresses
437 potential functional overlaps by characterizing model behavior across three scales:
438 micro-scale local sensitivity, domain-wide feature ranking, and regional heterogeneity.

439 **3.5.1 Micro-Scale Local Sensitivity**

440 We employ distinct attribution methods tailored to the hybrid inputs to capture
441 micro-scale responses. For the VPS, we apply gradient-based attribution, utilizing the
442 Input×Gradient method (Shrikumar et al., 2017) to quantify the sensitivity of AEC bias
443 correction to physicochemical profiles. Simultaneously, Cross-Attention weights are
444 extracted to map the interaction strength between the SFS and the VPS, revealing how

445 synoptic forcing modulates vertical profile rectifications. Furthermore, to understand
446 the model's internal decision-making, we analyze the learnable weights of the gated
447 feature fusion mechanism (detailed in Sect. 3.2.1). This analysis visualizes the altitude-
448 dependent prioritization among the four VPS components: physicochemical profiles,
449 height information, spatial coordinates, and temporal indices.

450 **3.5.2 Domain-wide Feature Ranking**

451 To assess the model's reliance on the overarching input feature groups (the VPS
452 and SFS), we perform permutation feature importance analysis (detailed in Sect. S7d).
453 By measuring the percentage increase in Mean Squared Error (MSE) when specific
454 groups are randomly shuffled, this method provides a domain-wide approach to identify
455 the fundamental predictors essential for AEC bias correction.

456 **3.5.3 Regional Heterogeneity**

457 Considering the spatial heterogeneity of aerosol sources, SHAP Analysis is used
458 to dissect regional dependencies and feature interactions. We employ a K-means
459 clustering strategy to construct a representative background dataset capturing diverse
460 atmospheric states (detailed in Sect. S8). SHAP values are computed for the designated
461 ROI to reveal how dominant AEC bias drivers shift under different environmental
462 regimes.

463

464 **4. Results and Discussion**

465 **4.1 Evaluation of the Transformer Model**

466 **4.1.1 Overall Predictive Performance and Temporal Generalization**

467 To quantitatively assess the model's robustness in capturing the non-linear
468 mapping between GEOS-Chem simulation biases and atmospheric states, we execute a
469 LOYO cross-validation strategy comprising three independent experiments (Table 1).
470 The Transformer achieves a high average R of 0.659 and a low MAE of 0.014 km⁻¹ on
471 the independent test years (Table 2). These metrics demonstrate robust predictive skill,
472 confirming that the model has successfully learned to reproduce the systematic

473 component of extinction biases from the input state variables. Notably, a comparison
474 with the internal validation results (Table S2) reveals that the model's performance on
475 the unseen test sets is comparable to—and in some metrics marginally superior to—
476 that on the validation sets. This consistency suggests that the Transformer architecture
477 has extracted time-invariant, physically meaningful representations of aerosol bias
478 mechanisms rather than overfitting to specific temporal anomalies in the training data.
479 The ability to generalize to years with distinct meteorological interactions underscores
480 the model's potential for operational bias correction.

481 **4.1.2 Seasonal Stability and Robustness**

482 We further examine the temporal stability of the model by analyzing monthly
483 variations in the predictive accuracy of the AEC simulation bias (Fig. 3). The model
484 exhibits a distinct seasonal pattern characterized by superior performance in winter and
485 a moderate decline in summer. During the winter months (December–February), R
486 consistently peaks above 0.7. This enhanced performance is attributed to the synergistic
487 effect of favorable meteorology and observational quality. Specifically, the lower solar
488 elevation angle in winter minimizes solar background noise, thereby enhancing the
489 Signal-to-Noise Ratio (SNR) of the CALIOP retrievals compared to the strong
490 background illumination present in summer (Zhen et al., 2024). Additionally, the stable
491 boundary layer in winter confines aerosols to lower altitudes (Xiong et al., 2026),
492 creating sharper vertical gradients that are physically more distinct for the network to
493 capture. In contrast, a discernible decline in performance occurs during the summer
494 (June–August) over EA. This reduction implies a compound mechanism driven by both
495 data scarcity and observational uncertainty. First, the decline coincides with a sharp
496 decrease in the effective sample size (Fig. 3a, gray bars). This is mechanically linked
497 to the Asian Summer Monsoon, where frequent cloud cover necessitates the exclusion
498 of a significant volume of cloud-contaminated CALIOP profiles (Winker et al., 2009;
499 Winker et al., 2013; Vernier et al., 2011), thereby reducing the representativeness of
500 training data for complex convective scenarios. Second, and more critically, the

501 inherently lower SNR in summer observations imposes a theoretical ceiling on point-
502 to-point correlation metrics. Since random noise in the validation target (CALIOP)
503 cannot be physically predicted, it naturally degrades the R, even if the model correctly
504 retrieves the underlying aerosol signal.

505 Crucially, despite the fluctuations in linear correlation driven by these external
506 sampling and observational constraints, the model demonstrates remarkable stability in
507 correcting systematic biases. Figure 3c illustrates that the monthly mean bias remains
508 tightly constrained within $\pm 0.01 \text{ km}^{-1}$ throughout the year, exhibiting negligible
509 seasonal drift even during the challenging summer months. This decoupling of metrics
510 implies that while random noise (reflected in lower R) increases in summer due to
511 complex meteorology and reduced SNR, the model does not introduce systematic
512 artifacts. This conclusion is further supported by internal validation results (Fig. S2),
513 which confirm that performance fluctuations are a response to data quality rather than
514 intrinsic model instability. Moreover, detailed monthly density scatter plots (Figs. S3–
515 S5) visually corroborate this robustness, revealing that the majority of predictions
516 remain tightly clustered around the 1:1 identity line, independent of the season.

517 **4.1.3 Vertical Profile Precision and Height-Dependent Performance**

518 Given the critical importance of vertical stratification in radiative forcing
519 calculations, we further scrutinize the model's performance as a function of altitude. A
520 distinct advantage of this study, unlike traditional bias correction methods limited to
521 column-integrated parameters, lies in its capability to finely resolve vertical aerosol
522 structures. As evidenced by the vertical profiles of evaluation metrics (Fig. 4a), the
523 model achieves peak performance within the bulk of the PBL (0.5–1.5 km), where R
524 consistently exceeds 0.7. This altitude range corresponds to the region with the heaviest
525 aerosol loading and the most complex chemical composition (Xiong et al., 2026; Jiang
526 et al., 2024). This superior skill suggests that the Transformer's self-attention
527 mechanism effectively captures the steep vertical gradients and pollutant accumulation
528 patterns driven by boundary layer dynamics. Furthermore, the NRMSE (Fig. 4b)

529 remains suppressed below 5% throughout the entire 0–6 km column. This low error
530 magnitude indicates that the model maintains consistent relative predictive accuracy
531 even in the cleaner free troposphere, avoiding the generation of spurious artifacts often
532 seen in DL applications on sparse data. Finally, the vertical profile of mean bias (Fig.
533 4c) fluctuates narrowly around zero at all altitude levels. This confirms the model's low
534 systematic bias in the vertical dimension, ensuring that the correction process mitigates
535 existing simulation errors without introducing new artificial biases.

536 **4.1.4 Spatial Generalization and Bias Reproduction**

537 Beyond capturing vertical structures, the capacity to resolve the spatial
538 heterogeneity of systematic biases is vital for correcting 3D aerosol fields. In the
539 primary study domain (EA), the Transformer demonstrates high precision in
540 reproducing the complex spatial bias modes of the original GEOS-Chem simulation
541 (Fig. 5, columns 1–3). Specifically, the model accurately captures the systematic
542 underestimation over major anthropogenic and biomass burning source regions,
543 including the NCP, IGP, and Indochina Peninsula. Over regions like the IGP, this
544 negative simulation bias is primarily driven by the underrepresentation of local biofuel
545 and agricultural emissions in traditional inventories (Mcduffie et al., 2020), coupled
546 with simplified aerosol mixing state assumptions that underestimate extinction
547 enhancement under high humidity (Burgos et al., 2020; Zhai et al., 2021). Furthermore,
548 the model's excessive numerical diffusion, a common limitation in CTMs, artificially
549 dilutes the strong near-surface pollutant accumulation bounded by local topography
550 (e.g., the Himalayas) (Eastham and Jacob, 2017). The GC-TF framework effectively
551 identifies and mitigates these state-dependent underestimations. Additionally, it
552 rectifies the biases over natural dust sources like the Taklamakan Desert. Conversely, it
553 correctly identifies regions of systematic overestimation, predominantly located over
554 the remote Western Pacific Ocean, the high-altitude Tibetan Plateau, and high-latitude
555 terrestrial regions (e.g., Siberia). These capabilities suggest that the model effectively
556 differentiates between bias regimes associated with distinct environments: it mitigates

557 the systematic overestimation in clean background regions while concurrently
558 compensating for the underestimation of source intensities in high-loading regions.

559 However, a localized area of strong positive AEC simulation bias (GEOS-Chem
560 overestimation) appears in Central China in the 2019 target map (Fig. 5c), which is not
561 fully reproduced by the prediction (Fig. 5g). We attribute this discrepancy primarily to
562 observational sparsity and the episodic nature of the bias. Specifically, this region
563 corresponds to a significantly lower density of valid CALIOP samples compared to the
564 surrounding domain (Fig. S6), likely resulting from retrieval limitations associated with
565 complex terrain and frequent cloud cover. Furthermore, monthly decomposition reveals
566 that this elevated annual mean AEC simulation bias is predominantly driven by extreme
567 values in January (Fig. S7), representing a transient winter episode specific to the 2019
568 test year. In such data-sparse regimes, the physics-informed Transformer model yields
569 conservative predictions, suggesting that it prioritizes learning generalized physical
570 laws over overfitting to localized outliers or specific interannual anomalies under-
571 represented in the training distribution.

572 Crucially, the fourth column of Figure 5 (2018 NA) presents a rigorous "out-of-
573 domain" generalization test, where the model trained exclusively on EA data is directly
574 applied to NA. Despite distinct differences in emission inventories and meteorological
575 backgrounds between the two continents, the model exhibits remarkable spatial
576 transferability. It successfully predicts the systematic underestimation over the Eastern
577 United States and the overestimation over coastal areas (e.g., the Gulf of Mexico and
578 the Atlantic coast), mirroring the actual GEOS-Chem AEC bias patterns (Target). This
579 successful spatial extrapolation strongly suggests that the physics-informed
580 Transformer model has learned the universal physical mapping between comprehensive
581 atmospheric state variables (detailed in Table S1) and CTM simulation biases, rather
582 than merely overfitting to the geographical coordinates or specific emission patterns of
583 the EA training domain.

584 **4.1.5 Sensitivity to Observational Uncertainties**

585 As discussed in Section 3.1, using satellite retrievals as the learning target
586 inherently absorbs CALIOP's systematic uncertainties. To quantify how this
587 observational limitation impacts the reliability of our framework, we conduct a
588 perturbation-based sensitivity analysis (detailed in Sect. S13). We retrain the GC-TF
589 model by artificially injecting a $\pm 5\%$ systematic perturbation into the CALIOP AEC
590 learning target.

591 Table S3 and Figure S17 demonstrate that this systematic perturbation induces
592 only a narrow envelope of variation in the corrected AEC profiles. The absolute shift in
593 the mean bias fluctuates tightly between 0.001 and 0.004 km^{-1} , and the perturbed
594 predictive RMSE (0.040 km^{-1}) consistently outperforms the original GEOS-Chem
595 simulation (0.052 km^{-1}) by a large margin. This confirms that while observational
596 uncertainties theoretically bound the absolute precision, the physics-informed
597 Transformer does not uncontrollably amplify these errors, ensuring the robustness of
598 the data-driven correction.

599 **4.1.6 Methodological Benchmarking and Structural Necessity**

600 To justify the architectural complexity and isolate the sources of performance
601 gains, we conduct comprehensive benchmarking and ablation studies using the
602 independent 2017 test dataset (Table S5). When trained with identical GEOS-Chem and
603 MERRA-2 predictors, the proposed Transformer significantly outperforms
604 conventional machine learning baselines. A standard Multilayer Perceptron (MLP) and
605 a 1-Dimensional Convolutional Neural Network (1D-CNN) yielded substantially lower
606 R ($R=0.083$ and 0.540 , respectively) compared to the Transformer ($R=0.666$). This
607 performance gap confirms that global sequence modeling via self-attention is critical
608 for capturing the long-range vertical coupling of atmospheric aerosols—such as
609 boundary layer-to-free troposphere exchange—which localized convolutions or point-
610 wise networks fail to resolve.

611 Furthermore, ablation experiments confirm that the performance enhancements
612 are intrinsically linked to our structural designs. Removing the Gated Feature Fusion or

613 the Cross-Attention module noticeably degrades predictive accuracy (Table S5). More
614 importantly, beyond statistical improvements, these modules are physically
615 indispensable. They transition the framework from a black-box predictor into a
616 diagnostic tool, providing the explicit attention weights necessary to quantify height-
617 dependent physical drivers (Sect. 4.5.1) and surface environmental modulations (Sect.
618 4.5.3).

619 **4.2 Evaluation of Corrected GEOS-Chem Simulations**

620 **4.2.1 Correction of Systematic Biases in AEC Magnitude**

621 To quantify the efficacy of the GEOS-Chem corrected by Transformer (GC-TF)
622 model in correcting the magnitude of the AEC, we first compare the overall statistical
623 relationship between simulated values and CALIOP observations across three
624 independent test years from 2017 to 2019 (Fig. 6). The original GEOS-Chem simulation
625 AEC exhibits a dispersed distribution around the 1:1 identity line, with R ranging only
626 from 0.50 to 0.53 and RMSE remaining high at 0.052–0.055 km⁻¹. Notably, the low
627 linear regression slopes (0.46–0.51) of the original simulation indicate a tendency to
628 underestimate aerosol extinction intensity under high-loading conditions. In contrast,
629 after correction by the GC-TF model, the AEC data points converge significantly
630 toward the 1:1 line. The R for AEC improves to 0.66–0.73, the RMSE decreases by
631 approximately 25% (to 0.039–0.042 km⁻¹), and the regression slope recovers to 0.55–
632 0.60. These results demonstrate that the framework effectively reduces random biases
633 and realigns the dynamic range of simulated extinction with observations.

634 Despite these substantial statistical improvements, visual scatter remains in the
635 density plots. To rigorously quantify these discrepancies, an error envelope of ± 0.15
636 km⁻¹ is introduced in Figure 6(d–f). Statistical analysis indicates that outliers exceeding
637 this threshold account for only 1.20% of the total dataset. Further diagnostic analysis
638 (detailed in Sect. S10) reveals that these extreme deviations are not random noise but
639 exhibit distinct spatial clustering over major emission hotspots (e.g., the IGP, the NCP,
640 and the Indochina Peninsula), and are vertically confined within the PBL (<1.5 km

641 AGL). These residuals are primarily driven by representativeness errors: CALIOP's
642 narrow footprint captures transient, highly concentrated sub-grid aerosol plumes, which
643 are inherently smoothed out during the spatial averaging process across the coarse
644 $2^\circ \times 2.5^\circ$ grid of GEOS-Chem. Consequently, the GC-TF model captures the systematic,
645 state-dependent biases of the grid mean, rather than fitting stochastic sub-grid extremes.

646 It is acknowledged that the high proportion of clean background samples (e.g., in
647 the upper troposphere) contributes to the overall correlation metrics. To rigorously
648 assess the model's capability in capturing effective aerosol signals—rather than merely
649 fitting the zero-value baseline—we conduct a threshold-based sensitivity analysis (Fig.
650 S9). As the extinction threshold increases from 0.00 to 0.20 km^{-1} , effectively filtering
651 out background noise and isolating optically thick aerosol layers, the GC-TF model
652 consistently outperforms the original GEOS-Chem simulation across all three
653 independent test years. Although the R values naturally decline as the sample size
654 shrinks to focus exclusively on extreme pollution events (indicated by the declining
655 gray dashed line in Fig. S9), the corrected results maintain a persistent performance
656 advantage over the original simulation. This confirms that the framework effectively
657 rectifies structural biases in high-AEC regimes and that its performance gains are not
658 merely artifacts of correctly predicting clean background states.

659 Further analysis of the vertical structure reveals more complex characteristics of
660 the model AEC bias. The annual mean vertical extinction profiles for the three test years
661 (Fig. 7) reveal a phenomenon: although the low slope in the scatter plots implies an
662 "underestimation" of strong signals, the annual mean profiles reveal that the original
663 GEOS-Chem exhibits a systematic "overestimation" relative to CALIOP observations
664 within the boundary layer ($<2 \text{ km}$). This apparent contradiction between macroscopic
665 statistical metrics and the vertical mean state actually exposes the typical "excessive
666 diffusion" issue in CTM simulations: the model struggles to capture the peaks of
667 extreme pollution events (leading to regression slopes <1) while systematically
668 overestimating widespread background aerosol concentrations (resulting in higher

669 intercepts and a systematic overestimation of the mean profile). The GC-TF model
670 successfully addresses this by performing a bidirectional correction: mitigating the
671 systemic overestimation in background regions while recovering the high-loading
672 signals attenuated by model diffusion. In particular, the corrected results neither
673 introduce spurious artifacts nor result in over-smoothing, accurately preserving vertical
674 variation trends consistent with observations even in the free troposphere where aerosol
675 loading is low.

676 It is important to note that while the absolute magnitude of the residual error (i.e.,
677 the remaining bias of the corrected AEC relative to observations) remains highest in the
678 near-surface layer (0–1 km) due to the significantly higher aerosol base loading in the
679 PBL (Fig. 7), the GC-TF model demonstrates its most critical contribution in this 0–1
680 km layer. It effectively bridges the gap between original simulations and observations,
681 reducing the mean AEC simulation bias by 33%–95% across the independent test years
682 (Fig. 7). Seasonal analysis (Fig. S10) further confirms that the model robustly reduces
683 simulation biases in the near-surface layer, regardless of the season. This substantial
684 reduction in near-surface bias is particularly vital for accurately deriving surface PM_{2.5}
685 concentrations and assessing aerosol health impacts.

686 The model's capacity to capture spatial heterogeneity is further validated through
687 regional analysis (Figs. S11–13) and explicit vertical bias profiles (Fig. S14). Rather
688 than merely learning a globally uniform bias factor, the GC-TF model exhibits
689 significant state-dependent adaptability. In the anthropogenic-dominated NCP and IGP,
690 as well as the dust-dominated Taklamakan Desert, where the original model shows
691 significant underestimation (Figs. S11–13a, b, c), the GC-TF model successfully
692 enhances the AEC to match observations, effectively pulling the negative bias profiles
693 back toward the zero-reference line (Fig. S14a–c). Additionally, in the Indochina
694 Peninsula, GEOS-Chem exhibits a spurious extinction peak near 0.8 km (Fig. S11d)
695 likely due to mischaracterized injection heights of biomass burning smoke. The GC-TF
696 model significantly attenuates this spurious peak. Conversely, over the relatively clean

697 Western Pacific, the model effectively reduces simulated values to address
698 overestimation (Fig. S11f). This ability to adaptively adjust the correction direction—
699 enhancing in polluted regions while suppressing in clean marine environments—
700 confirms the model's sensitivity to diverse underlying surfaces and emission regimes.

701 **4.2.2 Restoration of Zonal Mean and Longitudinal Vertical Structures**

702 To further evaluate the model's precision in resolving the macroscopic spatial-
703 vertical structure of AEC, we analyze the zonal mean vertical distribution of AEC over
704 EA (70°E–150°E) for the 2019 test year (Fig. 8). CALIOP observations (Fig. 8a)
705 identify a prominent aerosol high-loading belt concentrated between 20°N and 30°N,
706 corresponding to major anthropogenic sources in South and East Asia. This aerosol
707 layer is predominantly confined to the lower troposphere below 2 km, with a high-
708 extinction core concentrated within the lowest 1 km. In contrast, the original GEOS-
709 Chem simulation (Fig. 8b) exhibits a characteristic "excessive diffusion" bias: the high-
710 extinction layer is vertically over-extended (reaching above 3 km) and meridionally
711 spread into the clean tropical regions south of 10°N, resulting in a southward
712 displacement of the pollution center. The GC-TF model successfully rectifies these
713 biases by re-centering the high-concentration core to the observed 25°N latitude and
714 effectively constraining the vertical extent of the aerosol layer. By constraining the
715 vertical extent of aerosols, the model reduces the spurious diffusion into the free
716 troposphere and restores the peak extinction intensity suppressed by model smoothing.

717 Figure 9 further illustrates the annual mean longitudinal vertical cross-sections of
718 AEC along two key latitudinal transects (38.0°N and 40.0°N). These transects capture
719 the transition from continental dust sources and anthropogenic centers to downwind
720 marine regions. (1) Along the 38.0°N transect: CALIOP data (Fig. 9a) reveal two
721 distinct high-extinction cores: the Taklamakan Desert (75°E–85°E) and the NCP
722 (115°E–120°E). The original GEOS-Chem model (Fig. 9c) almost completely fails to
723 capture the intense near-surface dust accumulation in the Taklamakan region—likely
724 due to uncertainties in dust emission schemes or terrain smoothing effects in the

725 CTM—and severely underestimates the core intensity over the NCP. The GC-TF model
726 (Fig. 9e) successfully recovers the missing dust signal and sharpens the anthropogenic
727 core over the NCP, restoring high extinction values ($>0.16 \text{ km}^{-1}$) within the 0–1 km
728 layer to match observations. (2) Along the 40.0°N transect: This profile highlights
729 model performance over Northeast Asia and the Sea of Japan. CALIOP detects a
730 concentrated high-extinction core over North Korea ($\sim 127^\circ\text{E}$). While the original model
731 (Fig. 9d) significantly underestimates this peak, the GC-TF (Fig. 9f) effectively
732 captures this local anthropogenic hotspot. Notably, the original GEOS-Chem exhibits
733 unphysical aerosol "blobs" over the Sea of Japan (135°E – 138°E) and near 148°E , which
734 are unsupported by observations. The GC-TF model effectively suppresses these model
735 artifacts, ensuring that the extinction distribution in the downwind marine regions
736 maintains physical consistency with CALIOP observations.

737 **4.2.3 Correction of AOD and Assessment of Spatial Generalization**

738 Figure 10 presents a comprehensive evaluation of the GC-TF model's performance
739 in correcting column-integrated AOD biases over both the primary study domain (EA)
740 and an independent generalization domain (NA). By comparing CALIOP observations,
741 original GEOS-Chem simulations, and the GC-TF model results, we elucidate the
742 model's efficacy in reproducing spatial heterogeneity and improving statistical
743 consistency.

744 Within the EA training domain, although the original GEOS-Chem simulation
745 (Figs. 10a2, b2, c2) captures the macroscopic features of aerosol distribution, it exhibits
746 significant systematic biases. Specifically, it tends to underestimate AOD intensity over
747 major anthropogenic source regions (the NCP and the IGP) and biomass burning
748 hotspots (the Indochina Peninsula), while simultaneously introducing spurious
749 background aerosols over the cleaner Tibetan Plateau and Western Pacific. In contrast,
750 the GC-TF model (Figs. 10a3, b3, c3) significantly sharpens spatial gradients. The
751 corrected AOD fields show high agreement with CALIOP observations (Figs. 10a1, b1,
752 c1), effectively recovering high-value centers in polluted regions while suppressing

753 false positives in clean areas. Statistical evaluation further confirms this improvement:
754 while the original simulation shows dispersed scatter plots with low slopes (0.65–0.74),
755 the GC-TF corrected data tightly converge onto the 1:1 identity line. The R improves
756 from 0.80–0.84 to 0.91–0.93, the RMSE decreases by approximately 26%–40%, and
757 the regression slope recovers to 0.82–0.99 (Figs. 10a5, b5, c5). The temporal
758 consistency observed from 2017 to 2019 indicates that the model has learned stable
759 physical mapping relationships rather than overfitting to specific meteorological years.

760 Crucially, the evaluation over the NA domain (Fig. 10d) provides compelling
761 evidence of the model's spatial generalization capability. Despite the significantly lower
762 AOD magnitude and distinct emission characteristics compared to EA, the GC-TF
763 model demonstrates robust transferability. The original GEOS-Chem simulation over
764 NA (Figs. 10d2, d4) shows poor agreement with observations ($R=0.31$, slope=0.18),
765 indicating severe deficiencies in capturing regional aerosol variability. Specifically, it
766 underestimates anthropogenic pollution sources in the Eastern US (Fig. 10d1) and
767 exhibits spurious high-AOD trails over the Gulf of Mexico and the East Coast, likely
768 due to excessive transport or overestimated sea salt. Applying the GC-TF model—
769 trained exclusively on EA data—to this unseen region (Figs. 10d3, d5) yields a
770 substantial performance leap: R more than doubles to 0.70, and the slope improves to
771 0.45. Spatially, the model successfully recovers the smoothed pollution peaks in the
772 Eastern US and corrects the oceanic regions to clean background levels, consistent with
773 CALIOP. This bidirectional correction capability—enhancing underestimated
774 terrestrial signals while suppressing overestimated oceanic backgrounds—strongly
775 suggests that the physics-informed Transformer framework has captured the universal
776 physical linkages between atmospheric states and simulation biases, rather than merely
777 memorizing the geographical features of the EA training domain.

778 **4.3 Mechanisms of Cross-Continental Transferability**

779 The robust generalization capability demonstrated in the NA domain relies on the
780 universality of atmospheric physical laws. While EA and NA differ vastly in emission

781 intensities and aerosol regimes, core physicochemical processes governing aerosol
782 lifecycles remain consistent. The GC-TF model recognizes familiar synoptic patterns
783 and successfully transfers these learned physical constraints across continents. This
784 capability is well evidenced by its bidirectional correction over distinct underlying
785 surfaces. Over the Eastern United States, the model mitigates the Eulerian smearing
786 effect (Rastigejev et al., 2010; Eastham and Jacob, 2017). It restores sharp spatial
787 gradients and high-intensity anthropogenic pollution cores. Over marine regions like
788 the Gulf of Mexico, it effectively suppresses spurious background aerosols often driven
789 by excessive transport or sea-salt overestimation. The model dynamically utilizes
790 multidimensional atmospheric variables to physically constrain spatial distributions
791 rather than applying a simple uniform correction factor.

792 Despite these capabilities, the overall correction performance in NA ($R=0.70$)
793 remains statistically lower than in the EA training domain ($R=0.93$). We hypothesize
794 that this performance gap originates from a fundamental domain shift in aerosol
795 composition. The NA atmosphere features lower background concentrations and a
796 significantly higher fraction of biogenic Secondary Organic Aerosols (SOA) (Goldstein
797 et al., 2009). The optical properties and hygroscopicity of these organic species differ
798 fundamentally from the sulfate-nitrate-dust mixtures dominating EA (Crawford et al.,
799 2021).

800 To quantitatively verify this impact, we further evaluate the model performance
801 stratified by CALIOP aerosol subtypes over NA (Table S4). The results reveal a clear
802 divergence in the model's corrective capability across distinct aerosol regimes. For dust-
803 dominated regimes, the model effectively mitigates GEOS-Chem's systematic
804 underestimation, enhancing the regression slope from 0.21 to 0.32 and increasing R
805 from 0.41 to 0.50. This confirms that the physical constraints governing dust extinction
806 and vertical transport learned in EA translate reliably to the NA domain. In contrast, the
807 model yields negligible improvements for the SOA-dominated continental regime.
808 Although total mass concentrations are provided as predictors, the specific

809 thermodynamic-to-optical mapping learned in EA—typically dominated by the high
810 hygroscopic growth of inorganic salts—is less applicable to the complex, weakly
811 hygroscopic biogenic SOA prevalent in NA. The stagnant RMSE and R in the SOA
812 group suggest that without locally representative training samples to capture the unique
813 mass extinction efficiencies and refractive indices of NA-specific organic species, the
814 data-driven framework maintains a conservative correction. This ultimately limits the
815 overall precision gain across the NA background.

816 **4.4 Case Studies: Vertical Structure and Temporal Evolution During High Aerosol** 817 **Loading Periods**

818 To thoroughly evaluate the GC-TF model’s capability in resolving complex
819 vertical AEC stratification and capturing high-frequency pollution dynamics, we
820 conduct a composite analysis of representative high-loading episodes identified by
821 CALIOP over three distinct aerosol regimes (details in Sect. 2.3).

822 In the Taklimakan Desert (Fig. 11a), the original GEOS-Chem simulation exhibits
823 a nearly vertical extinction profile with extremely low values, indicating that the CTM
824 fails to simulate the significant aerosol extinction layer observed by CALIOP. In
825 contrast, the GC-TF model effectively recovers the extinction signal in this region by
826 leveraging multidimensional input atmospheric state variables (including
827 meteorological fields and background chemical composition). Its profile shape shows
828 superior agreement with satellite observations, largely retrieving the "missing signal"
829 of the original simulation. In Kanpur, a region dominated by anthropogenic pollution
830 (Fig. 11b), the original model fails to accurately capture the magnitude and vertical
831 gradient of the pollution layer below 3.5 km. The GC-TF model, while correcting
832 baseline errors, reshapes the vertical distribution pattern, yielding a vertical decrement
833 trend that aligns closely with observational reality. Figure 11c reveals critical structural
834 biases during a biomass burning event in the Indochina Peninsula. The original GEOS-
835 Chem simulation presents an "inverted" vertical gradient, where the extinction peak
836 appears at a height of 2.5 km rather than near the surface. This bias is likely associated

837 with uncertainties in the parameterization of biomass burning Plume Injection Height
838 in the CTM, suggesting the model erroneously transports surface smoke into the free
839 troposphere (Paugam et al., 2016). The GC-TF model successfully identifies this
840 physical process bias; by significantly enhancing AEC below 2.0 km, it restores a near-
841 surface high-loading pattern consistent with observations, while maintaining
842 reasonable simulation magnitudes in the free troposphere.

843 In addition to the instantaneous vertical structure, verifying the temporal
844 continuity of the correction results is equally crucial. Given the spatiotemporal sparsity
845 of CALIOP observations, we utilize ground-based high-frequency AERONET AOD
846 data to further evaluate model performance. A critical concern regarding DL models
847 trained on polar-orbiting satellite data is the potential overfitting to the sensor's limited
848 twice-daily sampling timing (e.g., ~01:30 and 13:30 local time for CALIOP). However,
849 the continuous AOD time series output by the GC-TF model demonstrates superior
850 trend consistency with the high-frequency AERONET observations throughout all
851 daylight hours. Figure 11d-e shows that the corrected model successfully captures the
852 dynamic diurnal evolution and phase fluctuations of aerosols. Specifically, Figure 11d
853 shows that during the study period in Kanpur, the original GEOS-Chem simulation
854 generally underestimates aerosol loading, and the curve exhibits overly smooth
855 characteristics, lacking response to high-frequency fluctuations. In contrast, the GC-TF
856 model closely tracks these dynamic variations. Notably, between May 1 and May 2, the
857 original simulation shows significant overestimation, whereas the GC-TF model
858 successfully adjusts the predicted values back to levels closer to observations. During
859 the active fire period in Nong Khai (Fig. 11e), the original model severely
860 underestimates the AOD magnitude. The GC-TF model significantly elevates the
861 simulation baseline and captures the phase of diurnal variation trends well (e.g., the
862 fluctuations around 07:00 UTC during February 22–24). This empirical evidence
863 confirms that by conditioning the bias correction on meteorology-driven diurnal
864 processes (as discussed in Sect. 3.1), the framework robustly generalizes across the

865 entire diurnal cycle and avoids overfitting to specific CALIOP overpass times.

866 However, its predicted peak amplitudes remain significantly lower than the
867 extreme values observed by AERONET. This dampening of extreme peaks likely stems
868 from the spatial scale mismatch between the gridded model ($2^\circ \times 2.5^\circ$) and ground-based
869 point observations, which causes local extreme emissions to be averaged out within the
870 grid. Nonetheless, the GC-TF model demonstrates significant improvement over the
871 original CTM in reproducing meteorology-driven pollution accumulation and
872 dispersion processes.

873 **4.5 Interpretability Analysis**

874 To move beyond statistical performance and elucidate the underlying physical
875 mappings learned by the correction framework, we employ a hierarchical diagnostic
876 approach to quantify feature contributions. This section and the subsequent analysis are
877 based entirely on the independent test dataset, ensuring that the interpretations reflect
878 the model's generalized physical representations on unseen data.

879 **4.5.1 Domain-Wide Reliance and Altitude-Dependent Prioritization**

880 To understand how the model resolves 3D aerosol fields, we first examine its
881 overarching reliance on different information streams. Domain-wide permutation
882 feature importance (Fig. S15) unambiguously establishes the foundational role of
883 physical priors: randomly permuting the physicochemical profile induces a dramatic
884 196.1% increase in MSE. This confirms that the physicochemical profiles provided by
885 the CTM remain the indispensable physical foundation, determining the absolute
886 Magnitude of the AEC. In contrast, spatial, temporal, and height components function
887 as modulating variables, refining this baseline across diverse environmental regimes.

888 Further analysis of the gated feature fusion weights (Fig. 12) reveals that the model
889 effectively adapts its prioritization mechanism based on atmospheric stratification. In
890 the near-surface layer (<0.5 km), the model assigns the highest weight to
891 physicochemical profiles, aligning with the physical reality that extinction near the
892 surface is predominantly controlled by local emissions and immediate thermodynamic

893 states (Jiang et al., 2024; Xiong et al., 2026). As height increases to the boundary layer
894 transition zone (0.5–1.0 km), a strategic shift occurs. The reliance on physicochemical
895 profiles diminishes while the weight of spatial coordinates increases significantly. This
896 region typically corresponds to the entrainment zone or the top of the PBL, where
897 CTMs are prone to vertical diffusion errors (Eastham and Jacob, 2017; Rastigejev et al.,
898 2010; Lin and Mcelroy, 2010). The model mitigates these uncertainties by leveraging
899 spatial priors to constrain potential diffusion biases. In the mid-lower troposphere (1.0–
900 3.5 km), the contribution of temporal indices exhibits distinct peaks around 1.5 km and
901 2.8 km. The 1.5 km peak corresponds to the typical maximum daytime PBLH in EA
902 (Guo et al., 2016; Kim, 2022), while the 2.8 km peak aligns with the active layer for
903 long-range transport (Uno et al., 2009). This demonstrates the model’s utilization of
904 temporal cues to capture the diurnal evolution of the PBL and seasonal transport events.
905 In the free troposphere (>3.5 km), aerosol variability is vertically decoupled from
906 surface processes and driven primarily by large-scale advection (Weinzierl et al., 2017;
907 Val Martin et al., 2013; Uno et al., 2009). The model successfully captures this
908 decoupling, shifting its strategy to rely heavily on spatial coordinates to constrain
909 background aerosol fields. Explicit height encoding maintains a consistently high
910 contribution throughout the entire column, serving as a critical vertical positioning
911 anchor.

912 **4.5.2 Vertical Attribution of Local State Variables**

913 Following the domain-wide ranking, we utilize gradient-based attribution (Fig. 13)
914 to dissect the specific variables within the VPS driving AEC bias correction across
915 altitudes. These drivers are organized into thermodynamic constraints, particulate
916 compositions, and dynamic factors.

917 First, thermodynamic variables serve as the primary constraints for rectifying the
918 vertical AEC structure. Temperature (T) consistently acts as the dominant driver within
919 the PBL, with attribution scores exceeding 0.20. This suggests that the model implicitly
920 diagnoses atmospheric stability and vertical lapse rate—factors often mischaracterized

921 in CTMs—to rectify biases associated with turbulent mixing (Lin and McElroy, 2010).
922 Concurrently, Relative Humidity (RH) functions as a critical driver for aerosol optical
923 properties. Its contribution is coupled with explicit hygroscopic growth factors (e.g.,
924 `AerHygroscopicGrowth_SO42-`), enabling the model to fine-tune the AEC and correct
925 non-linear hygroscopic parameterization errors under high-humidity conditions
926 (Burgos et al., 2020; Zhai et al., 2021).

927 Second, particulate mass concentrations act as the fundamental determinants of
928 aerosol loading. In the lower troposphere (<1.5 km), PM_{2.5} and PM₁₀ consistently rank
929 among the top drivers. The model also demonstrates a physically stratified recognition
930 of aerosol types; for instance, the importance of sea salt aerosol (`AerMassSAL`) is
931 confined strictly to the marine boundary layer (<1.5 km) and decays rapidly aloft,
932 accurately reflecting the vertical distribution of coarse-mode marine aerosols (Bian et
933 al., 2019; Murphy et al., 2019).

934 Finally, dynamic variables exhibit a persistent influence aloft. Unlike precursor
935 concentrations, which decay sharply with height, the importance of wind components
936 (U, V) remains relatively stable in the free troposphere (>2.0 km). This indicates that
937 as height increases, the model shifts its focus from local accumulation to large-scale
938 advection, utilizing wind fields to rectify background biases induced by long-range
939 transport.

940 **4.5.3 Synoptic Modulation via Surface Constraints**

941 While the VPS determines the baseline extinction, the cross-attention mechanism
942 enables the model to utilize the SFS to modulate the vertical bias correction (Fig. 14).
943 This process operates through distinct physical pathways.

944 First, the model employs a robust dynamic representation to constrain transport
945 and mixing efficiency. The consistently high attention weights of 10 m wind
946 components (U10M, V10M) reflect the use of near-surface wind speed as a proxy for
947 synoptic flow patterns. The model identifies the dominance of meridional transport in
948 the EA monsoon region, assigning slightly higher importance to meridional winds

949 (V10M) to capture dominant pollutant exchange pathways (Ding et al., 2009; Choi et
950 al., 2024; Uno et al., 2009). By identifying prevailing dynamic regimes, the model
951 effectively addresses CTM biases related to pollutant accumulation under stagnant
952 conditions (Kim et al., 2024; An et al., 2019) and numerical diffusion under strong
953 advection (Rastigejev et al., 2010; Eastham and Jacob, 2017). More critically, the cross-
954 attention weights reveal a vertical partitioning of turbulence drivers. Thermodynamic
955 drivers (HFLUX, LAI) peak at the surface and decay upward, diagnosing surface
956 buoyancy fluxes. In contrast, mechanical drivers (USTAR, Z0M) increase and plateau
957 with height. This distinction implies the model successfully evaluates vertical
958 entrainment potential, assessing whether mechanical shear is sufficient to transport
959 pollutants across capping inversions.

960 Second, radiative and surface boundary conditions are leveraged to correct
961 parameterization biases. The model senses solar input by distinguishing between direct
962 (PARDR) and diffuse (PARDF) photosynthetically active radiation, capturing
963 variations in photochemistry and secondary aerosol formation (Guenther et al., 2012).
964 Furthermore, snow mass (SNOMAS) emerges as a key predictor in the lowest layers.
965 The model identifies snow-covered surfaces as indicators of a strongly stable boundary
966 layer prone to temperature inversions. This allows for the targeted correction of over-
967 dilution biases often found in CTMs (Lin and Mcelroy, 2010; Holtslag et al., 2013),
968 effectively capturing high-concentration signals that are typically artificially smoothed
969 by minimal diffusion threshold constraints.

970 **4.5.4 Regional Heterogeneity of Bias Drivers**

971 To reveal the model's predictive behavior under diverse environmental contexts,
972 we conduct SHAP analysis (Fig. 15) to identify region-specific correction patterns
973 adapted to distinct underlying surfaces and emissions.

974 In regions dominated by anthropogenic and biomass burning emissions (NCP, IGP,
975 and Indochina), the model leverages radiative components to diagnose atmospheric
976 turbidity. A striking commonality is the high ranking of diffuse radiation (PARDF),

977 often surpassing the direct component (PARDR). This reflects the physical
978 phenomenon where high aerosol loading enhances scattering and increases the diffuse
979 fraction of solar radiation (Mercado et al., 2009; Che et al., 2018). Furthermore, the
980 model differentiates surface energy partitioning: in the humid, vegetated IGP and
981 Indochina, it prioritizes latent heat flux (EFLUX) to gauge hygroscopic growth and wet
982 removal potential; conversely, in the urbanized NCP, it relies more heavily on sensible
983 heat flux (HFLUX), consistent with the high Bowen ratio of urban surfaces (Miao et
984 al., 2009) where thermal turbulence dominates vertical dispersion.

985 In the dust-dominated Taklamakan Desert, the model captures a coupled
986 mechanism driven by thermodynamic instability and dynamic uplift. Incident
987 shortwave flux (SWGDN) and direct radiation (PARDR) play a dominant role,
988 indicating that the model identifies clear-sky, high-solar-input conditions as
989 prerequisites for thermal instability. Crucially, this is coupled with dynamic descriptors:
990 combining low vegetation indices (GRN, identifying erodible bare soil), high 10m wind
991 speeds (providing surface shear stress) (Shao et al., 2011), and a preference for coarse-
992 mode PM₁₀ over PM_{2.5}. This confirms the model has learned the physical prerequisites
993 for wind-driven dust emission in arid regions.

994 Finally, over the marine environment of the Western Pacific, the model shifts to a
995 latent heat-driven mode. Latent heat flux (EFLUX) defines the moisture supply at the
996 air-sea interface, controlling marine aerosol hygroscopicity. Additionally, the model
997 captures sea spray generation by linking near-surface wind speeds (V10M) with land-
998 sea masking indicators (GRN), recognizing that mechanically generated sea salt
999 aerosols (Grythe et al., 2014) and their subsequent hygroscopic evolution are the
1000 primary drivers of AEC variability over open water.

1001 **4.6 Diagnostic Insights for Refining GEOS-Chem Parameterizations**

1002 The interpretability analysis in Section 4.5 demonstrates that the GC-TF model
1003 captures physically meaningful relationships rather than merely fitting statistical noise.
1004 While directly translating data-driven feature sensitivities into concrete code

1005 modifications remains challenging without further sensitivity simulations, this
1006 transparency allows the framework to serve as a valuable hypothesis-generation tool. It
1007 highlights potential structural uncertainties in CTMs and points toward targeted
1008 refinements in physical parameterizations.

1009 **4.6.1 Diagnosing Thermodynamic Parameterization Deficiencies**

1010 The model heavily relies on temperature and HFLUX to correct AEC profiles (Sect.
1011 4.5.2, 4.5.4), which suggests potential uncertainties in diagnosing PBLH and turbulent
1012 mixing intensity within the GEOS-Chem non-local boundary layer scheme. Given that
1013 HFLUX drives surface buoyancy and directly modulates the vertical eddy diffusion
1014 coefficient, the widespread excessive diffusion biases observed in the lower
1015 troposphere indicate that the model may overestimate thermal turbulence under certain
1016 stability conditions. In highly urbanized regions like the NCP, the acute sensitivity to
1017 HFLUX implies that current surface energy balance calculations struggle to resolve the
1018 distinct thermodynamic properties of urban canopies. Future model development could
1019 benefit from constraining stability functions within the vertical diffusion module or
1020 coupling a dedicated urban canopy model to better represent sensible heat partitioning.

1021 **4.6.2 Refining Emission and Formation Schemes via Environmental Proxies**

1022 The cross-attention weights, which reveal how synoptic forcing modulates vertical
1023 aerosol profiles (Sect. 4.5.3, 4.5.4), highlight potentially inadequately parameterized
1024 mechanisms in current emission and chemical modules. Over the Taklamakan Desert,
1025 the model explicitly pairs greenness fraction with surface wind speed to capture dust
1026 extinction. This suggests that the GEOS-Chem dust emission scheme might struggle to
1027 accurately parameterize threshold friction velocity over complex bare soils, indicating
1028 that the non-linear response of wind-blown dust to surface shear stress and soil
1029 erodibility likely requires recalibration. Similarly, high sensitivity to diffuse radiation
1030 in the biomass burning region of Indochina points to potentially under-represented SOA
1031 formation. Given that high aerosol loading enhances diffuse radiation and alters
1032 photolysis rates, the data-driven model likely leverages diffuse radiation as a proxy for

1033 accelerated photochemical aging. This highlights a need to optimize SOA yield
1034 parameterizations and refine biomass burning plume injection heights to capture rapid
1035 aerosol evolution in dense smoke.

1036 **4.6.3 Bridging Data-Driven Interpretation with CTM Development**

1037 Beyond statistical bias correction, this study highlights the utility of physics-
1038 informed DL for model diagnosis. By decoupling the contributions of meteorology and
1039 aerosol composition, the framework verifies that CTMs provide a robust
1040 physicochemical baseline, yet exhibit uncertainties in representing the complex, non-
1041 linear interactions between aerosols and meteorology. The correction strategies derived
1042 from the data-driven model offer valuable diagnostic clues. Identifying specific
1043 environmental proxies that govern simulation biases bridges the gap between data-
1044 driven retrieval and deterministic modeling, ultimately guiding the targeted integration
1045 of neglected physical constraints into future parameterization schemes.

1046 **4.7 Model Limitations and Scope of Application**

1047 As a supervised bias-correction framework, the model relies on state-dependent
1048 mapping, meaning its performance is fundamentally constrained by the predictive
1049 signals available in the input features. The framework excels at correcting systematic,
1050 parameterization-driven bias. For instance, it successfully restores the underestimated
1051 dust plumes in the Taklamakan Desert by leveraging wind speed, clear-sky radiation,
1052 and vegetation indices as physical proxies for actual dust emission conditions (Sect.
1053 4.5.4).

1054 However, the model possesses limited capacity to compensate for entirely missing
1055 physical processes. If a highly localized or stochastic event is completely absent from
1056 the prescribed emission inventory and produces no corresponding anomalies in the
1057 input meteorological or chemical precursor fields, the model lacks the necessary
1058 physical constraints to capture the resulting aerosol plume. In such scenarios, the
1059 correction remains strictly bounded by the prior information provided by the GEOS-
1060 Chem and MERRA2.

1061

1062 **5. Conclusions**

1063 This study proposes a physics-informed Transformer DL framework that generates
1064 high-precision 3D AEC fields by bridging the gap between CTM simulations and
1065 CALIOP satellite observations. Functioning as a supervised bias-correction model
1066 rather than a DA system, this framework learns a state-dependent mapping to rectify
1067 systematic simulation AEC bias. Distinct from traditional bias correction methods that
1068 rely solely on passive remote sensing imagery or treat the model as a black box, this
1069 framework explicitly integrates physicochemical vertical structural priors (e.g., AEPs
1070 and species concentrations) from GEOS-Chem and meteorological constraints from
1071 MERRA-2. By constructing a dual-stream architecture featuring Gated Feature Fusion
1072 and Cross-Attention mechanisms, the model effectively captures the complex, non-
1073 linear dependencies between atmospheric states and AEC simulation biases. The
1074 primary conclusions are as follows:

1075 First, the framework significantly improves the precision of AEC vertical profiles,
1076 systematically correcting the systematic biases inherent in Eulerian CTMs. Extensive
1077 LOYO cross-validation over EA (2017–2019) demonstrates that the R for AEC
1078 evaluated against CALIOP observations increases from 0.49–0.53 in the original
1079 GEOS-Chem simulation to 0.66–0.73, while the RMSE is reduced by approximately
1080 25%. Vertically, the model achieves optimal performance within the PBL (0.5–1.5 km),
1081 with R consistently exceeding 0.7 and NRMSE remaining below 5%. The framework
1082 effectively mitigates the excessive diffusion issue common in CTMs, rectifying the
1083 spurious southward displacement of pollution centers, restoring smoothed high-
1084 intensity extinction signals in anthropogenic and dust source regions, and suppressing
1085 spurious overestimations in the clean free troposphere and over marine regions.
1086 Crucially, threshold-based sensitivity analysis confirms that these performance gains
1087 are robust even when focusing exclusively on optically thick aerosol layers.
1088 Consequently, this vertical rectification leads to a substantial improvement in column-

1089 integrated AOD, with the R relative to CALIOP increasing from 0.80–0.84 to 0.91–
1090 0.93 across the EA domain, ensuring consistency between resolved AEC vertical
1091 structures and the total aerosol load. Moreover, validation against high-frequency
1092 ground-based AERONET measurements confirms the framework's superiority over the
1093 original GEOS-Chem simulation in capturing the dynamic temporal evolution of
1094 pollution episodes, bridging the observational gaps inherent to the sparse sampling of
1095 polar-orbiting satellites.

1096 Second, the model exhibits robust cross-continental transferability, indicating that
1097 it has internalized universal physical laws rather than overfitting to regional training
1098 characteristics. When applied directly to the NA domain—a region with distinct
1099 emission structures and lower aerosol loading—without any retraining, the model
1100 successfully reproduces the spatial AEC simulation bias patterns of GEOS-Chem. The
1101 R for column-integrated AOD compared with CALIOP retrievals in this region
1102 improves significantly from 0.31 (original) to 0.70 (corrected), further verifying the
1103 physical consistency and transferability of the established mapping between
1104 atmospheric states and AEC simulation biases.

1105 Third, by integrating interpretable DL techniques, this study advances beyond
1106 standard bias correction to serve as a diagnostic framework for physical mechanisms.
1107 Attribution analysis reveals that the model identifies AEC simulation bias drivers with
1108 clear physical significance: (1) In the PBL, the heavy reliance on temperature and
1109 HFLUX highlights potential uncertainties in vertical eddy diffusion coefficients within
1110 stability-dependent mixing schemes; (2) Over dust source regions, the paired use of
1111 vegetation indices and wind speed suggests the need to recalibrate threshold friction
1112 velocity and soil erodibility; (3) In biomass burning regions, the sensitivity to diffuse
1113 radiation points to under-represented SOA yields and photochemical aging processes;
1114 (4) In marine regions, the utilization of latent heat flux and surface wind implies
1115 uncertainties in sea-salt generation functions and hygroscopic growth.

1116 In summary, this study not only confirms the effectiveness of the physics-informed

1117 Transformer in deriving high-precision 3D aerosol fields to support radiative forcing
1118 assessments but also highlights its potential as a diagnostic tool for CTMs. However, it
1119 is important to acknowledge that as a supervised bias-correction framework, the
1120 absolute accuracy of the corrected AEC profiles is inherently bounded by the systematic
1121 uncertainties of the baseline CALIOP retrievals. While the model effectively mitigates
1122 the structural and parameterization-driven biases within GEOS-Chem, any intrinsic
1123 observational noise or systematic retrieval errors propagate into the correction, setting
1124 a theoretical ceiling on the absolute precision of the data-driven product. Despite this
1125 constraint, the interpretability analysis provides developers with actionable physical
1126 insights, highlighting a shift in the integration of DL with physical modeling. Rather
1127 than serving solely as a post-processing tool for bias correction, the framework
1128 functions as a diagnostic mechanism to identify structural model deficiencies and guide
1129 the refinement of parameterization schemes in CTMs.

1130

1131 **Code and Data availability.** The GEOS-Chem model is available at [http://www.geos-](http://www.geos-chem.org)
1132 [chem.org](http://www.geos-chem.org). The CALIOP satellite data can be accessed via
1133 <https://subset.larc.nasa.gov/calipso>. The MERRA-2 data are available from the NASA
1134 Goddard Earth Sciences Data and Information Services Center
1135 (<https://disc.gsfc.nasa.gov/>). AERONET data can be obtained from
1136 <https://aeronet.gsfc.nasa.gov/>. The source code of the physics-informed Transformer
1137 model proposed in this study, and the trained weights, are available upon request from
1138 the corresponding author.

1139

1140 **Author contribution.** JX designed the research, developed the model methodology,
1141 conducted the simulations, performed the data analysis, and prepared the original draft.
1142 YW supervised the study, provided the computing resources, and revised the
1143 manuscript. JW revised the manuscript. YYW, MZ, MT, WD, JK, and LW provided
1144 technical support and reviewed the manuscript. All authors contributed to the

1145 interpretation of the results and the improvement of the paper.

1146

1147 **Competing Interests.** The contact author has declared that none of the authors has any
1148 competing interests.

1149

1150 **Acknowledgements.** This research was funded by the National Natural Science
1151 Foundation of China (Grant No. 42571377). Jun Wang's participation is made possible
1152 via the in-kind support (Lichtenberger Family Chair in Chemical Engineering) from the
1153 University of Iowa.

1154

1155 **References**

1156 An, Z., Huang, R. J., Zhang, R., Tie, X., Li, G., Cao, J., Zhou, W., Shi, Z., Han, Y., Gu,
1157 Z., and Ji, Y.: Severe haze in northern China: A synergy of anthropogenic
1158 emissions and atmospheric processes, *Proc. Natl. Acad. Sci. U.S.A.*, 116, 8657-
1159 8666, 10.1073/pnas.1900125116, 2019.

1160 Benedetti, A., Reid, J. S., Knippertz, P., Marsham, J. H., Di Giuseppe, F., Rémy, S.,
1161 Basart, S., Boucher, O., Brooks, I. M., Menut, L., Mona, L., Laj, P., Pappalardo,
1162 G., Wiedensohler, A., Baklanov, A., Brooks, M., Colarco, P. R., Cuevas, E., da
1163 Silva, A., Escribano, J., Flemming, J., Huneus, N., Jorba, O., Kazadzis, S., Kinne,
1164 S., Popp, T., Quinn, P. K., Sekiyama, T. T., Tanaka, T., and Terradellas, E.: Status
1165 and future of numerical atmospheric aerosol prediction with a focus on data
1166 requirements, *Atmos. Chem. Phys.*, 18, 10615-10643, 10.5194/acp-18-10615-
1167 2018, 2018.

1168 Bey, I., Jacob, D. J., Yantosca, R. M., Logan, J. A., Field, B. D., Fiore, A. M., Li, Q. B.,
1169 Liu, H. G. Y., Mickley, L. J., and Schultz, M. G.: Global modeling of tropospheric
1170 chemistry with assimilated meteorology: Model description and evaluation, *J.*
1171 *Geophys. Res.:Atmos.*, 106, 23073-23095, 10.1029/2001jd000807, 2001.

1172 Bian, H. S., Froyd, K., Murphy, D. M., Dibb, J., Darmenov, A., Chin, M., Colarco, P.

1173 R., da Silva, A., Kucsera, T. L., Schill, G., Yu, H. B., Bui, P., Dollner, M., Weinzierl,
1174 B., and Smirnov, A.: Observationally constrained analysis of sea salt aerosol in the
1175 marine atmosphere, *Atmos. Chem. Phys.*, 19, 10773-10785, 10.5194/acp-19-
1176 10773-2019, 2019.

1177 Bocquet, M., Pires, C. A., and Wu, L.: Beyond Gaussian Statistical Modeling in
1178 Geophysical Data Assimilation, *Mon. Wea. Rev.*, 138, 2997-3023,
1179 10.1175/2010mwr3164.1, 2010.

1180 Bond, T. C., Doherty, S. J., Fahey, D. W., Forster, P. M., Berntsen, T., DeAngelo, B. J.,
1181 Flanner, M. G., Ghan, S., Kärcher, B., Koch, D., Kinne, S., Kondo, Y., Quinn, P.
1182 K., Sarofim, M. C., Schultz, M. G., Schulz, M., Venkataraman, C., Zhang, H.,
1183 Zhang, S., Bellouin, N., Guttikunda, S. K., Hopke, P. K., Jacobson, M. Z., Kaiser,
1184 J. W., Klimont, Z., Lohmann, U., Schwarz, J. P., Shindell, D., Storelvmo, T.,
1185 Warren, S. G., and Zender, C. S.: Bounding the role of black carbon in the climate
1186 system: A scientific assessment, *J. Geophys. Res.:Atmos.*, 118, 5380-5552,
1187 10.1002/jgrd.50171, 2013.

1188 Burgos, M. A., Andrews, E., Titos, G., Benedetti, A., Bian, H. S., Buchard, V., Curci,
1189 G., Kipling, Z., Kirkevåg, A., Kokkola, H., Laakso, A., Letertre-Danczak, J., Lund,
1190 M. T., Matsui, H., Myhre, G., Randles, C., Schulz, M., van Noije, T., Zhang, K.,
1191 Alados-Arboledas, L., Baltensperger, U., Jefferson, A., Sherman, J., Sun, J. Y.,
1192 Weingartner, E., and Zieger, P.: A global model-measurement evaluation of
1193 particle light scattering coefficients at elevated relative humidity, *Atmos. Chem.*
1194 *Phys.*, 20, 10231-10258, 10.5194/acp-20-10231-2020, 2020.

1195 Che, H. Z., Qi, B., Zhao, H. J., Xia, X. G., Eck, T. F., Goloub, P., Dubovik, O., Estelles,
1196 V., Cuevas-Agulló, E., Blarel, L., Wu, Y. F., Zhu, J., Du, R. G., Wang, Y. Q., Wang,
1197 H., Gui, K., Yu, J., Zheng, Y., Sun, T. Z., Chen, Q. L., Shi, G. Y., and Zhang, X. Y.:
1198 Aerosol optical properties and direct radiative forcing based on measurements
1199 from the China Aerosol Remote Sensing Network (CARSNET) in eastern China,
1200 *Atmos. Chem. Phys.*, 18, 405-425, 10.5194/acp-18-405-2018, 2018.

1201 Chen, B., Song, Z., Pan, F., and Huang, Y.: Obtaining vertical distribution of PM_{2.5}
1202 from CALIOP data and machine learning algorithms, *Sci. Total Environ.*, 805,
1203 150338, 10.1016/j.scitotenv.2021.150338, 2022a.

1204 Chen, J., Jiang, Z., Li, R., Liao, C., Miyazaki, K., and Jones, D. B. A.: Large
1205 discrepancy between observed and modeled wintertime tropospheric NO₂
1206 variabilities due to COVID-19 controls in China, *Environ. Res. Lett.*, 17,
1207 10.1088/1748-9326/ac4ec0, 2022b.

1208 Chen, X., Wang, J., Xu, X. G., and Zhou, M.: Dust Aerosol Optical Centroid Height
1209 (AOCH) Over Bright Surface: First Retrieval From TROPOMI Oxygen A and B
1210 Absorption Bands, *IEEE Geosci. Remote Sensing Lett.*, 22,
1211 10.1109/lgrs.2025.3601046, 2025.

1212 Chimot, J., Veefkind, J. P., Vlemmix, T., and Levelt, P. F.: Spatial distribution analysis
1213 of the OMI aerosol layer height: a pixel-by-pixel comparison to CALIOP
1214 observations, *Atmos. Meas. Tech.*, 11, 2257-2277, 10.5194/amt-11-2257-2018,
1215 2018.

1216 Chinnam, N., Dey, S., Tripathi, S. N., and Sharma, M.: Dust events in Kanpur, northern
1217 India: Chemical evidence for source and implications to radiative forcing,
1218 *Geophys. Res. Lett.*, 33, 10.1029/2005gl025278, 2006.

1219 Choi, M., Park, J., Sung, M., and Ying, Q.: Long-Range Transport of Secondary
1220 Inorganic Aerosol from China to South Korea, *Environ. Sci. Technol. Lett.*, 11,
1221 1233-1238, 10.1021/acs.estlett.4c00852, 2024.

1222 Christensen, M. W., Jones, W. K., and Stier, P.: Aerosols enhance cloud lifetime and
1223 brightness along the stratus-to-cumulus transition, *Proc. Natl. Acad. Sci. U.S.A.*,
1224 117, 17591-17598, 10.1073/pnas.1921231117, 2020.

1225 Colarco, P. R., Kahn, R. A., Remer, L. A., and Levy, R. C.: Impact of satellite viewing-
1226 swath width on global and regional aerosol optical thickness statistics and trends,
1227 *Atmos. Meas. Tech.*, 7, 2313-2335, 10.5194/amt-7-2313-2014, 2014.

1228 Crawford, J. H., Ahn, J. Y., Al-Saadi, J., Chang, L., Emmons, L. K., Kim, J., Lee, G.,

1229 Park, J. H., Park, R. J., Woo, J. H., Song, C. K., Hong, J. H., Hong, Y. D., Lefer,
1230 B. L., Lee, M., Lee, T., Kim, S., Min, K. E., Yum, S. S., Shin, H. J., Kim, Y. W.,
1231 Choi, J. S., Park, J. S., Szykman, J. J., Long, R. W., Jordan, C. E., Simpson, I. J.,
1232 Fried, A., Dibb, J. E., Cho, S., and Kim, Y. P.: The Korea-United States Air Quality
1233 (KORUS-AQ) field study, *Elem. Sci. Anth.*, 9, 10.1525/elementa.2020.00163,
1234 2021.

1235 Daoud, N., Eltahan, M., and Elhennawi, A.: Aerosol Optical Depth Forecast over
1236 Global Dust Belt Based on LSTM, CNN-LSTM, CONV-LSTM and FFT
1237 Algorithms, 19th International Conference on Smart Technologies (IEEE
1238 EUROCON), Lviv, UKRAINE, Jul 06-08 2021, WOS:000728121700034, 186-
1239 191, 10.1109/eurocon52738.2021.9535571, 2021.

1240 Diner, D. J., Boland, S. W., Brauer, M., Bruegge, C., Burke, K. A., Chipman, R., Di
1241 Girolamo, L., Garay, M. J., Hasheminassab, S., Hyer, E., Jerrett, M., Jovanovic,
1242 V., Kalashnikova, O. V., Liu, Y., Lyapustin, A. I., Martin, R. V., Nastan, A., Ostro,
1243 B. D., Ritz, B., Schwartz, J., Wang, J., and Xu, F.: Advances in multiangle satellite
1244 remote sensing of speciated airborne particulate matter and association with
1245 adverse health effects: from MISR to MAIA, *J. Appl. Remote Sens.*, 12,
1246 10.1117/1.Jrs.12.042603, 2018.

1247 Ding, A. J., Wang, T., Xue, L. K., Gao, J., Stohl, A., Lei, H. C., Jin, D. Z., Ren, Y., Wang,
1248 X. Z., Wei, X. L., Qi, Y. B., Liu, J., and Zhang, X. Q.: Transport of north China air
1249 pollution by midlatitude cyclones: Case study of aircraft measurements in summer
1250 2007 (vol 114, D08304, 2007), *J. Geophys. Res.:Atmos.*, 114,
1251 10.1029/2009jd012339, 2009.

1252 Ding, S. G., Wang, J., and Xu, X. G.: Polarimetric remote sensing in oxygen A and B
1253 bands: sensitivity study and information content analysis for vertical profile of
1254 aerosols, *Atmos. Meas. Tech.*, 9, 2077-2092, 10.5194/amt-9-2077-2016, 2016.

1255 Dong, W., Tao, M., Xu, X., Wang, J., Wang, Y., Wang, L., Song, Y., Fan, M., and Chen,
1256 L.: Satellite Aerosol Retrieval From Multiangle Polarimetric Measurements:

1257 Information Content and Uncertainty Analysis, *IEEE Trans. Geosci. Remote*
1258 *Sensing*, 61, 1-13, 10.1109/tgrs.2023.3264554, 2023.

1259 Du, Q., Zhao, C., Zhang, M., Dong, X., Chen, Y., Liu, Z., Hu, Z., Zhang, Q., Li, Y.,
1260 Yuan, R., and Miao, S.: Modeling diurnal variation of surface PM_{2.5}
1261 concentrations over East China with WRF-Chem: impacts from boundary-layer
1262 mixing and anthropogenic emission, *Atmos. Chem. Phys.*, 20, 2839-2863,
1263 10.5194/acp-20-2839-2020, 2020.

1264 Dubovik, O., Herman, M., Holdak, A., Lapyonok, T., Tanré, D., Deuzé, J. L., Ducos, F.,
1265 Sinyuk, A., and Lopatin, A.: Statistically optimized inversion algorithm for
1266 enhanced retrieval of aerosol properties from spectral multi-angle polarimetric
1267 satellite observations, *Atmos. Meas. Tech.*, 4, 975-1018, 10.5194/amt-4-975-2011,
1268 2011.

1269 Eastham, S. D. and Jacob, D. J.: Limits on the ability of global Eulerian models to
1270 resolve intercontinental transport of chemical plumes, *Atmos. Chem. Phys.*, 17,
1271 2543-2553, 10.5194/acp-17-2543-2017, 2017.

1272 Fan, Y., Sun, L., Wang, Z., Pang, S., and Wei, J.: Unveiling diurnal aerosol layer height
1273 variability from space using deep learning, *ISPRS. J. Photogramm. Remote. Sens.*,
1274 229, 211-222, 10.1016/j.isprsjprs.2025.08.021, 2025.

1275 Ge, C., Wang, J., and Reid, J. S.: Mesoscale modeling of smoke transport over the
1276 Southeast Asian Maritime Continent: coupling of smoke direct radiative effect
1277 below and above the low-level clouds, *Atmos. Chem. Phys.*, 14, 159-174,
1278 10.5194/acp-14-159-2014, 2014.

1279 Geer, A. J.: Learning earth system models from observations: machine learning or data
1280 assimilation?, *Philos. Trans. R. Soc. A Math. Phys. Eng.*, 379,
1281 10.1098/rsta.2020.0089, 2021.

1282 Gelaro, R., McCarty, W., Suárez, M. J., Todling, R., Molod, A., Takacs, L., Randles, C.
1283 A., Darmenov, A., Bosilovich, M. G., Reichle, R., Wargan, K., Coy, L., Cullather,
1284 R., Draper, C., Akella, S., Buchard, V., Conaty, A., da Silva, A. M., Gu, W., Kim,

1285 G. K., Koster, R., Lucchesi, R., Merkova, D., Nielsen, J. E., Partyka, G., Pawson,
1286 S., Putman, W., Rienecker, M., Schubert, S. D., Sienkiewicz, M., and Zhao, B.:
1287 The Modern-Era Retrospective Analysis for Research and Applications, Version 2
1288 (MERRA-2), *J. Climate*, 30, 5419-5454, 10.1175/jcli-d-16-0758.1, 2017.

1289 Getzewich, B. J., Vaughan, M. A., Hunt, W. H., Avery, M. A., Powell, K. A., Tackett, J.
1290 L., Winker, D. M., Kar, J., Lee, K. P., and Toth, T. D.: CALIPSO lidar calibration
1291 at 532 nm: version 4 daytime algorithm, *Atmos. Meas. Tech.*, 11, 6309-6326,
1292 10.5194/amt-11-6309-2018, 2018.

1293 Giglio, L., Randerson, J. T., and van der Werf, G. R.: Analysis of daily, monthly, and
1294 annual burned area using the fourth-generation global fire emissions database
1295 (GFED4), *J. Geophys. Res. Biogeosci.*, 118, 317-328, 10.1002/jgrg.20042, 2013.

1296 Giles, D. M., Sinyuk, A., Sorokin, M. G., Schafer, J. S., Smirnov, A., Slutsker, I., Eck,
1297 T. F., Holben, B. N., Lewis, J. R., Campbell, J. R., Welton, E. J., Korkin, S. V., and
1298 Lyapustin, A. I.: Advancements in the Aerosol Robotic Network (AERONET)
1299 Version 3 database - automated near-real-time quality control algorithm with
1300 improved cloud screening for Sun photometer aerosol optical depth (AOD)
1301 measurements, *Atmos. Meas. Tech.*, 12, 169-209, 10.5194/amt-12-169-2019, 2019.

1302 Goldstein, A. H., Koven, C. D., Heald, C. L., and Fung, I. Y.: Biogenic carbon and
1303 anthropogenic pollutants combine to form a cooling haze over the southeastern
1304 United States, *Proc. Natl. Acad. Sci. U.S.A.*, 106, 8835-8840,
1305 10.1073/pnas.0904128106, 2009.

1306 Grythe, H., Ström, J., Krejci, R., Quinn, P., and Stohl, A.: A review of sea-spray aerosol
1307 source functions using a large global set of sea salt aerosol concentration
1308 measurements, *Atmos. Chem. Phys.*, 14, 1277-1297, 10.5194/acp-14-1277-2014,
1309 2014.

1310 Guenther, A. B., Jiang, X., Heald, C. L., Sakulyanontvittaya, T., Duhl, T., Emmons, L.
1311 K., and Wang, X.: The Model of Emissions of Gases and Aerosols from Nature
1312 version 2.1 (MEGAN2.1): an extended and updated framework for modeling

1313 biogenic emissions, *Geosci. Model Dev.*, 5, 1471-1492, 10.5194/gmd-5-1471-
1314 2012, 2012.

1315 Guo, J., He, J., Liu, H., Miao, Y., Liu, H., and Zhai, P.: Impact of various emission
1316 control schemes on air quality using WRF-Chem during APEC China 2014, *Atmos.*
1317 *Environ.*, 140, 311-319, 10.1016/j.atmosenv.2016.05.046, 2016.

1318 Handschuh, J., Erbertseder, T., Schaap, M., and Baier, F.: Estimating PM_{2.5} surface
1319 concentrations from AOD: A combination of SLSTR and MODIS, *Remote. Sens.*
1320 *Appl.*, 26, 10.1016/j.rsase.2022.100716, 2022.

1321 Henze, D. K., Hakami, A., and Seinfeld, J. H.: Development of the adjoint of GEOS-
1322 Chem, *Atmos. Chem. Phys.*, 7, 2413-2433, 10.5194/acp-7-2413-2007, 2007.

1323 Henze, D. K., Seinfeld, J. H., and Shindell, D. T.: Inverse modeling and mapping US
1324 air quality influences of inorganic PM_{2.5} precursor emissions using the adjoint of
1325 GEOS-Chem, *Atmos. Chem. Phys.*, 9, 5877-5903, 10.5194/acp-9-5877-2009,
1326 2009.

1327 Hoesly, R. M., Smith, S. J., Feng, L., Klimont, Z., Janssens-Maenhout, G., Pitkanen, T.,
1328 Seibert, J. J., Vu, L., Andres, R. J., Bolt, R. M., Bond, T. C., Dawidowski, L.,
1329 Kholod, N., Kurokawa, J.-i., Li, M., Liu, L., Lu, Z., Moura, M. C. P., O'Rourke, P.
1330 R., and Zhang, Q.: Historical (1750–2014) anthropogenic emissions of reactive
1331 gases and aerosols from the Community Emissions Data System (CEDS), *Geosci.*
1332 *Model Dev.*, 11, 369-408, 10.5194/gmd-11-369-2018, 2018.

1333 Holben, B. N., Eck, T. F., Slutsker, I., Tanre, D., Buis, J. P., Setzer, A., Vermote, E.,
1334 Reagan, J. A., Kaufman, Y. J., Nakajima, T., Lavenu, F., Jankowiak, I., and
1335 Smirnov, A.: AERONET - A federated instrument network and data archive for
1336 aerosol characterization, *Remote Sens. Environ.*, 66, 1-16, 10.1016/s0034-
1337 4257(98)00031-5, 1998.

1338 Holtslag, A. A. M., Svensson, G., Baas, P., Basu, S., Beare, B., Beljaars, A. C. M.,
1339 Bosveld, F. C., Cuxart, J., Lindvall, J., Steeneveld, G. J., Tjernström, M., and Van
1340 De Wiel, B. J. H.: Stable Atmospheric Boundary Layers and Diurnal Cycles:

1341 Challenges for Weather and Climate Models, *Bull. Am. Meteorol. Soc.*, 94, 1691-
1342 1706, 10.1175/bams-d-11-00187.1, 2013.

1343 Hong, Y. and Di Girolamo, L.: An Overview of Aerosol Properties in Clear and Cloudy
1344 Sky Based on CALIPSO Observations, *Earth Space Sci.*, 9,
1345 10.1029/2022ea002287, 2022.

1346 Hu, X. F., Waller, L. A., Lyapustin, A., Wang, Y. J., Al-Hamdan, M. Z., Crosson, W. L.,
1347 Estes, M. G., Estes, S. M., Quattrochi, D. A., Puttaswamy, S. J., and Liu, Y.:
1348 Estimating ground-level PM_{2.5} concentrations in the Southeastern United States
1349 using MAIAC AOD retrievals and a two-stage model, *Remote Sens. Environ.*, 140,
1350 220-232, 10.1016/j.rse.2013.08.032, 2014.

1351 Huang, J. T., Loría-Salazar, S., Deng, M., Lee, J., and Holmes, H. A.: Assessment of
1352 smoke plume height products derived from multisource satellite observations
1353 using lidar-derived height metrics for wildfires in the western US, *Atmos. Chem.*
1354 *Phys.*, 24, 3673-3698, 10.5194/acp-24-3673-2024, 2024.

1355 Huang, L., Jiang, J. H., Tackett, J. L., Su, H., and Fu, R.: Seasonal and diurnal variations
1356 of aerosol extinction profile and type distribution from CALIPSO 5 - year
1357 observations, *J. Geophys. Res.:Atmos.*, 118, 4572-4596, 10.1002/jgrd.50407,
1358 2013.

1359 Hunt, W. H., Winker, D. M., Vaughan, M. A., Powell, K. A., Lucker, P. L., and Weimer,
1360 C.: CALIPSO Lidar Description and Performance Assessment, *J. Atmos. Oceanic*
1361 *Technol.*, 26, 1214-1228, 10.1175/2009jtecha1223.1, 2009.

1362 Ichoku, C., Chu, D. A., Mattoo, S., Kaufman, Y. J., Remer, L. A., Tanré, D., Slutsker,
1363 I., and Holben, B. N.: A spatio-temporal approach for global validation and
1364 analysis of MODIS aerosol products, *Geophys. Res. Lett.*, 29,
1365 10.1029/2001gl013206, 2002.

1366 Jiang, X., Wang, Y., Wang, L., Tao, M., Wang, J., Zhou, M., Bai, X., and Gui, L.:
1367 Characteristics of Daytime - And - Nighttime AOD Differences Over China: A
1368 Perspective From CALIOP Satellite Observations and GEOS - Chem Model

1369 Simulations, *J. Geophys. Res.:Atmos.*, 129, 10.1029/2023jd039158, 2024.

1370 Kahn, R. A., Gaitley, B. J., Martonchik, J. V., Diner, D. J., Crean, K. A., and Holben,
1371 B.: Multiangle Imaging Spectroradiometer (MISR) global aerosol optical depth
1372 validation based on 2 years of coincident Aerosol Robotic Network (AERONET)
1373 observations - art. no. D10S04, *J. Geophys. Res.:Atmos.*, 110,
1374 10.1029/2004jd004706, 2005.

1375 Kaufman, Y. J., Tanré, D., and Boucher, O.: A satellite view of aerosols in the climate
1376 system, *Nature*, 419, 215-223, 10.1038/nature01091, 2002.

1377 Kim, H., Chen, X., Wang, J., Lu, Z. D., Zhou, M., Carmichael, G. R., Park, S. S., and
1378 Kim, J.: Aerosol layer height (ALH) retrievals from oxygen absorption bands:
1379 intercomparison and validation among different satellite platforms, GEMS, EPIC,
1380 and TROPOMI, *Atmos. Meas. Tech.*, 18, 327-349, 10.5194/amt-18-327-2025,
1381 2025.

1382 Kim, H., Park, R. J., Hong, S. Y., Park, D. H., Kim, S. W., Oak, Y. J., Feng, X., Lin, H.,
1383 and Fu, T. M.: A mixed layer height parameterization in a 3-D chemical transport
1384 model: Implications for gas and aerosol simulations, *Sci. Total Environ.*, 955,
1385 176838, 10.1016/j.scitotenv.2024.176838, 2024.

1386 Kim, K.-Y.: Diurnal and seasonal variation of planetary boundary layer height over East
1387 Asia and its climatic change as seen in the ERA-5 reanalysis data, *SN Appl. Sci.*,
1388 4, 10.1007/s42452-021-04918-5, 2022.

1389 Kim, M.-H., Omar, A. H., Tackett, J. L., Vaughan, M. A., Winker, D. M., Trepte, C. R.,
1390 Hu, Y., Liu, Z., Poole, L. R., Pitts, M. C., Kar, J., and Magill, B. E.: The CALIPSO
1391 version 4 automated aerosol classification and lidar ratio selection algorithm,
1392 *Atmos. Meas. Tech.*, 11, 6107-6135, 10.5194/amt-11-6107-2018, 2018.

1393 Kim, P. S., Jacob, D. J., Fisher, J. A., Travis, K., Yu, K., Zhu, L., Yantosca, R. M.,
1394 Sulprizio, M. P., Jimenez, J. L., Campuzano-Jost, P., Froyd, K. D., Liao, J., Hair,
1395 J. W., Fenn, M. A., Butler, C. F., Wagner, N. L., Gordon, T. D., Welti, A., Wennberg,
1396 P. O., Crouse, J. D., St. Clair, J. M., Teng, A. P., Millet, D. B., Schwarz, J. P.,

1397 Markovic, M. Z., and Perring, A. E.: Sources, seasonality, and trends of southeast
1398 US aerosol: an integrated analysis of surface, aircraft, and satellite observations
1399 with the GEOS-Chem chemical transport model, *Atmos. Chem. Phys.*, 15, 10411-
1400 10433, 10.5194/acp-15-10411-2015, 2015.

1401 Koch, D. and Del Genio, A. D.: Black carbon semi-direct effects on cloud cover: review
1402 and synthesis, *Atmos. Chem. Phys.*, 10, 7685-7696, 10.5194/acp-10-7685-2010,
1403 2010.

1404 Koffi, B., Schulz, M., Bréon, F. M., Griesfeller, J., Winker, D., Balkanski, Y., Bauer, S.,
1405 Berntsen, T., Chin, M., Collins, W. D., Dentener, F., Diehl, T., Easter, R., Ghan, S.,
1406 Ginoux, P., Gong, S., Horowitz, L. W., Iversen, T., Kirkevåg, A., Koch, D., Krol,
1407 M., Myhre, G., Stier, P., and Takemura, T.: Application of the CALIOP layer
1408 product to evaluate the vertical distribution of aerosols estimated by global models:
1409 AeroCom phase I results, *J. Geophys. Res.:Atmos.*, 117, 10.1029/2011jd016858,
1410 2012a.

1411 Koffi, B., Schulz, M., Bréon, F. M., Griesfeller, J., Winker, D., Balkanski, Y., Bauer, S.,
1412 Berntsen, T., Chin, M. A., Collins, W. D., Dentener, F., Diehl, T., Easter, R., Ghan,
1413 S., Ginoux, P., Gong, S. L., Horowitz, L. W., Iversen, T., Kirkevåg, A., Koch, D.,
1414 Krol, M., Myhre, G., Stier, P., and Takemura, T.: Application of the CALIOP layer
1415 product to evaluate the vertical distribution of aerosols estimated by global models:
1416 AeroCom phase I results, *J. Geophys. Res.:Atmos.*, 117, 10.1029/2011jd016858,
1417 2012b.

1418 Koffi, B., Schulz, M., Breon, F. M., Dentener, F., Steensen, B. M., Griesfeller, J., Winker,
1419 D., Balkanski, Y., Bauer, S. E., Bellouin, N., Berntsen, T., Bian, H., Chin, M., Diehl,
1420 T., Easter, R., Ghan, S., Hauglustaine, D. A., Iversen, T., Kirkevag, A., Liu, X.,
1421 Lohmann, U., Myhre, G., Rasch, P., Seland, O., Skeie, R. B., Steenrod, S. D., Stier,
1422 P., Tackett, J., Takemura, T., Tsigaridis, K., Vuolo, M. R., Yoon, J., and Zhang, K.:
1423 Evaluation of the aerosol vertical distribution in global aerosol models through
1424 comparison against CALIOP measurements: AeroCom phase II results, *J.*

1425 Geophys. Res.:Atmos., 121, 7254-7283, 10.1002/2015JD024639, 2016.

1426 Li, T. W., Shen, H. F., Yuan, Q. Q., Zhang, X. C., and Zhang, L. P.: Estimating Ground-
1427 Level PM_{2.5} by Fusing Satellite and Station Observations: A Geo-Intelligent Deep
1428 Learning Approach, Geophys. Res. Lett., 44, 11985-11993,
1429 10.1002/2017gl075710, 2017.

1430 Li, X. N., Cheng, X., Wu, W. J., Wang, Q. H., Tong, Z. Y., Zhang, X. Q., Deng, D. H.,
1431 and Li, Y. H.: Forecasting of bioaerosol concentration by a Back Propagation
1432 neural network model, Sci. Total Environ., 698, 10.1016/j.scitotenv.2019.134315,
1433 2020.

1434 Liang, M., Han, Z., Li, J., Sun, Y., Liang, L., and Li, Y.: Radiative effects and feedbacks
1435 of anthropogenic aerosols on boundary layer meteorology and fine particulate
1436 matter during the COVID-19 lockdown over China, Sci. Total Environ., 862,
1437 160767, 10.1016/j.scitotenv.2022.160767, 2023.

1438 Lin, J. T. and McElroy, M. B.: Impacts of boundary layer mixing on pollutant vertical
1439 profiles in the lower troposphere: Implications to satellite remote sensing, Atmos.
1440 Environ., 44, 1726-1739, 10.1016/j.atmosenv.2010.02.009, 2010.

1441 Liu, J., Zheng, Y., Li, Z., Flynn, C., and Cribb, M.: Seasonal variations of aerosol optical
1442 properties, vertical distribution and associated radiative effects in the Yangtze
1443 Delta region of China, J. Geophys. Res.:Atmos., 117, 10.1029/2011jd016490,
1444 2012.

1445 Lu, Q., Liu, C., Zhao, D. L., Zeng, C., Li, J., Lu, C. S., Wang, J. D., and Zhu, B.:
1446 Atmospheric heating rate due to black carbon aerosols: Uncertainties and impact
1447 factors, Atmos. Res., 240, 10.1016/j.atmosres.2020.104891, 2020.

1448 Lu, Z., Wang, J., Chen, X., Xu, X., Zhou, M., Fu, D., and Jiang, J. H.: First Retrieval of
1449 Aerosol Vertical Profile With Passive Remote Sensing: Part 1. Development of
1450 Algorithm Theoretical Basis, J. Geophys. Res.:Atmos., 130,
1451 10.1029/2025jd044332, 2025a.

1452 Lu, Z. D., Wang, J., Chen, X., Xu, X. G., Zhou, M., Fu, D. J., and Jiang, J. H.: First

1453 Retrieval of Aerosol Vertical Profile With Passive Remote Sensing: Part 1.
1454 Development of Algorithm Theoretical Basis, *J. Geophys. Res.:Atmos.*, 130,
1455 10.1029/2025jd044332, 2025b.

1456 Lundberg, S. M. and Lee, S. I.: A Unified Approach to Interpreting Model Predictions,
1457 31st Annual Conference on Neural Information Processing Systems (NIPS), Long
1458 Beach, CA, Dec 04-09 2017, WOS:000452649404081, 2017.

1459 Lv, B., Hu, Y., Chang, H. H., Russell, A. G., and Bai, Y.: Improving the Accuracy of
1460 Daily PM_{2.5} Distributions Derived from the Fusion of Ground-Level
1461 Measurements with Aerosol Optical Depth Observations, a Case Study in North
1462 China, *Environ. Sci. Technol.*, 50, 4752-4759, 10.1021/acs.est.5b05940, 2016.

1463 McDuffie, E. E., Smith, S. J., O'Rourke, P., Tibrewal, K., Venkataraman, C., Marais, E.
1464 A., Zheng, B., Crippa, M., Brauer, M., and Martin, R. V.: A global anthropogenic
1465 emission inventory of atmospheric pollutants from sector- and fuel-specific
1466 sources (1970–2017): an application of the Community Emissions Data System
1467 (CEDS), *Earth Syst. Sci. Data*, 12, 3413-3442, 10.5194/essd-12-3413-2020, 2020.

1468 Mehta, S. K., Ananthavel, A., Velu, V., Prabhakaran, T., Pandithurai, G., and Rao, D.
1469 N.: Characteristics of elevated aerosol layer over the Indian east coast,
1470 Kattankulathur (12.82°N, 80.04°E): A northeast monsoon region, *Sci. Total
1471 Environ.*, 886, 10.1016/j.scitotenv.2023.163917, 2023.

1472 Mercado, L. M., Bellouin, N., Sitch, S., Boucher, O., Huntingford, C., Wild, M., and
1473 Cox, P. M.: Impact of changes in diffuse radiation on the global land carbon sink,
1474 *Nature*, 458, 1014-U1087, 10.1038/nature07949, 2009.

1475 Miao, S. G., Chen, F., Lemone, M. A., Tewari, M., Li, Q. C., and Wang, Y. C.: An
1476 Observational and Modeling Study of Characteristics of Urban Heat Island and
1477 Boundary Layer Structures in Beijing, *J. Appl. Meteorol. Climatol.*, 48, 484-501,
1478 10.1175/2008jamc1909.1, 2009.

1479 Misra, A., Gaur, A., Bhattu, D., Ghosh, S., Dwivedi, A. K., Dalai, R., Paul, D., Gupta,
1480 T., Tare, V., Mishra, S. K., Singh, S., and Tripathi, S. N.: An overview of the

1481 physico-chemical characteristics of dust at Kanpur in the central Indo-Gangetic
1482 basin, *Atmos. Environ.*, 97, 386-396, 10.1016/j.atmosenv.2014.08.043, 2014.

1483 Munroe, D. K., Wolfenbarger, S. R., Calder, C. A., Shi, T., Xiao, N., Lam, C. Q., and Li,
1484 D.: The relationships between biomass burning, land-cover/-use change, and the
1485 distribution of carbonaceous aerosols in mainland Southeast Asia: a review and
1486 synthesis, *J. Land Use Sci.*, 3, 161-183, 10.1080/17474230802332241, 2008.

1487 Murphy, D. M., Froyd, K. D., Bian, H. S., Brock, C. A., Dibb, J. E., DiGangi, J. P.,
1488 Diskin, G., Dollner, M., Kupc, A., Scheuer, E. M., Schill, G. P., Weinzierl, B.,
1489 Williamson, C. J., and Yu, P. F.: The distribution of sea-salt aerosol in the global
1490 troposphere, *Atmos. Chem. Phys.*, 19, 4093-4104, 10.5194/acp-19-4093-2019,
1491 2019.

1492 Myhre, G., Samset, B. H., Schulz, M., Balkanski, Y., Bauer, S., Berntsen, T. K., Bian,
1493 H., Bellouin, N., Chin, M., Diehl, T., Easter, R. C., Feichter, J., Ghan, S. J.,
1494 Hauglustaine, D., Iversen, T., Kinne, S., Kirkevåg, A., Lamarque, J. F., Lin, G.,
1495 Liu, X., Lund, M. T., Luo, G., Ma, X., van Noije, T., Penner, J. E., Rasch, P. J.,
1496 Ruiz, A., Seland, O., Skeie, R. B., Stier, P., Takemura, T., Tsigaridis, K., Wang, P.,
1497 Wang, Z., Xu, L., Yu, H., Yu, F., Yoon, J. H., Zhang, K., Zhang, H., and Zhou, C.:
1498 Radiative forcing of the direct aerosol effect from AeroCom Phase II simulations,
1499 *Atmos. Chem. Phys.*, 13, 1853-1877, 10.5194/acp-13-1853-2013, 2013.

1500 Nanda, S., de Graaf, M., Veefkind, J. P., Sneep, M., ter Linden, M., Sun, J. Y. T., and
1501 Levelt, P. F.: A first comparison of TROPOMI aerosol layer height (ALH) to
1502 CALIOP data, *Atmos. Meas. Tech.*, 13, 3043-3059, 10.5194/amt-13-3043-2020,
1503 2020.

1504 Nanda, S., Veefkind, J. P., de Graaf, M., Sneep, M., Stammes, P., de Haan, J. F., Sanders,
1505 A. F. J., Apituley, A., Tuinder, O., and Levelt, P. F.: A weighted least squares
1506 approach to retrieve aerosol layer height over bright surfaces applied to GOME-2
1507 measurements of the oxygen A band for forest fire cases over Europe, *Atmos.*
1508 *Meas. Tech.*, 11, 3263-3280, 10.5194/amt-11-3263-2018, 2018.

1509 Nguyen, D.-L., Czech, H., Pieber, S. M., Schnelle-Kreis, J., Steinbacher, M., Orasche,
1510 J., Henne, S., Popovicheva, O. B., Abbaszade, G., Engling, G., Bukowiecki, N.,
1511 Nguyen, N.-A., Nguyen, X.-A., and Zimmermann, R.: Carbonaceous aerosol
1512 composition in air masses influenced by large-scale biomass burning: a case study
1513 in northwestern Vietnam, *Atmos. Chem. Phys.*, 21, 8293-8312, 10.5194/acp-21-
1514 8293-2021, 2021.

1515 Pashayi, M., Satari, M., and Shahraki, M. M.: Multi-layer retrieval of aerosol optical
1516 depth in the troposphere using SEVIRI data: a case study of the European
1517 continent, *Atmos. Meas. Tech.*, 18, 1415-1439, 10.5194/amt-18-1415-2025, 2025.

1518 Paugam, R., Wooster, M., Freitas, S., and Martin, M. V.: A review of approaches to
1519 estimate wildfire plume injection height within large-scale atmospheric chemical
1520 transport models, *Atmos. Chem. Phys.*, 16, 907-925, 10.5194/acp-16-907-2016,
1521 2016.

1522 Rastigejev, Y., Park, R., Brenner, M. P., and Jacob, D. J.: Resolving intercontinental
1523 pollution plumes in global models of atmospheric transport, *J. Geophys.*
1524 *Res.:Atmos.*, 115, 10.1029/2009jd012568, 2010.

1525 Reichstein, M., Camps-Valls, G., Stevens, B., Jung, M., Denzler, J., Carvalhais, N., and
1526 Prabhat: Deep learning and process understanding for data-driven Earth system
1527 science, *Nature*, 566, 195-204, 10.1038/s41586-019-0912-1, 2019.

1528 Samset, B. H., Myhre, G., Schulz, M., Balkanski, Y., Bauer, S., Berntsen, T. K., Bian,
1529 H., Bellouin, N., Diehl, T., Easter, R. C., Ghan, S. J., Iversen, T., Kinne, S.,
1530 Kirkevåg, A., Lamarque, J. F., Lin, G., Liu, X., Penner, J. E., Seland, O., Skeie, R.
1531 B., Stier, P., Takemura, T., Tsigaridis, K., and Zhang, K.: Black carbon vertical
1532 profiles strongly affect its radiative forcing uncertainty, *Atmos. Chem. Phys.*, 13,
1533 2423-2434, 10.5194/acp-13-2423-2013, 2013.

1534 Sanders, A. F. J., de Haan, J. F., Sneep, M., Apituley, A., Stammes, P., Viteitez, M. O.,
1535 Tilstra, L. G., Tuinder, O. N. E., Koning, C. E., and Veefkind, J. P.: Evaluation of
1536 the operational Aerosol Layer Height retrieval algorithm for Sentinel-5 Precursor:

1537 application to O2 A band observations from GOME-2A, *Atmos. Meas. Tech.*, 8,
1538 4947-4977, 10.5194/amt-8-4947-2015, 2015.

1539 Sekiyama, T. T., Tanaka, T. Y., Shimizu, A., and Miyoshi, T.: Data assimilation of
1540 CALIPSO aerosol observations, *Atmos. Chem. Phys.*, 10, 39-49, 10.5194/acp-10-
1541 39-2010, 2010.

1542 Shao, Y. P., Wyrwoll, K. H., Chappell, A., Huang, J. P., Lin, Z. H., McTainsh, G. H.,
1543 Mikami, M., Tanaka, T. Y., Wang, X. L., and Yoon, S.: Dust cycle: An emerging
1544 core theme in Earth system science, *Aeolian Res.*, 2, 181-204,
1545 10.1016/j.aeolia.2011.02.001, 2011.

1546 Shi, S. S., Zhu, B., Lu, W., Yan, S. Q., Fang, C. W., Liu, X. H., Liu, D. Y., and Liu, C.:
1547 Estimation of radiative forcing and heating rate based on vertical observation of
1548 black carbon in Nanjing, China, *Sci. Total Environ.*, 756,
1549 10.1016/j.scitotenv.2020.144135, 2021.

1550 Shrikumar, A., Greenside, P., and Kundaje, A.: Learning Important Features Through
1551 Propagating Activation Differences, 34th International Conference on Machine
1552 Learning, Sydney, AUSTRALIA, Aug 06-11 2017, WOS:000683309503025,
1553 2017.

1554 Singh, R. P., Dey, S., Tripathi, S. N., Tare, V., and Holben, B.: Variability of aerosol
1555 parameters over Kanpur, northern India, *J. Geophys. Res.:Atmos.*, 109,
1556 10.1029/2004jd004966, 2004.

1557 Song, X. W., Wu, D., Jin, L. N., Xu, Y. Y., Chen, X., and Li, Q.: Aerosol Toxicokinetics:
1558 A Framework for Unraveling Toxicological Dynamics from Air to the Body,
1559 *Environ. Sci. Technol.*, 59, 6379-6386, 10.1021/acs.est.5c00751, 2025.

1560 Stier, P., Seinfeld, J. H., Kinne, S., and Boucher, O.: Aerosol absorption and radiative
1561 forcing, *Atmos. Chem. Phys.*, 7, 5237-5261, 10.5194/acp-7-5237-2007, 2007.

1562 Tsay, S.-C., Hsu, N. C., Lau, W. K. M., Li, C., Gabriel, P. M., Ji, Q., Holben, B. N.,
1563 Judd Welton, E., Nguyen, A. X., Janjai, S., Lin, N.-H., Reid, J. S., Boonjawat, J.,
1564 Howell, S. G., Huebert, B. J., Fu, J. S., Hansell, R. A., Sayer, A. M., Gautam, R.,

1565 Wang, S.-H., Goodloe, C. S., Miko, L. R., Shu, P. K., Loftus, A. M., Huang, J.,
1566 Kim, J. Y., Jeong, M.-J., and Pantina, P.: From BASE-ASIA toward 7-SEAS: A
1567 satellite-surface perspective of boreal spring biomass-burning aerosols and clouds
1568 in Southeast Asia, *Atmos. Environ.*, 78, 20-34, 10.1016/j.atmosenv.2012.12.013,
1569 2013.

1570 Uno, I., Eguchi, K., Yumimoto, K., Takemura, T., Shimizu, A., Uematsu, M., Liu, Z. Y.,
1571 Wang, Z. F., Hara, Y., and Sugimoto, N.: Asian dust transported one full circuit
1572 around the globe, *Nat. Geosci.*, 2, 557-560, 10.1038/ngeo583, 2009.

1573 Val Martin, M., Heald, C. L., Ford, B., Prenni, A. J., and Wiedinmyer, C.: A decadal
1574 satellite analysis of the origins and impacts of smoke in Colorado, *Atmos. Chem.*
1575 *Phys.*, 13, 7429-7439, 10.5194/acp-13-7429-2013, 2013.

1576 Vaswani, A., Shazeer, N., Parmar, N., Uszkoreit, J., Jones, L., Gomez, A. N., Kaiser, L.,
1577 and Polosukhin, I.: Attention Is All You Need, 31st Annual Conference on Neural
1578 Information Processing Systems (NIPS), Long Beach, CA, Dec 04-09 2017,
1579 WOS:000452649406008, 2017.

1580 Vernier, J. P., Thomason, L. W., Pommereau, J. P., Bourassa, A., Pelon, J., Garnier, A.,
1581 Hauchecorne, A., Blanot, L., Trepte, C., Degenstein, D., and Vargas, F.: Major
1582 influence of tropical volcanic eruptions on the stratospheric aerosol layer during
1583 the last decade, *Geophys. Res. Lett.*, 38, n/a-n/a, 10.1029/2011gl047563, 2011.

1584 Wang, J., Park, S., Zeng, J., Ge, C., Yang, K., Carn, S., Krotkov, N., and Omar, A. H.:
1585 Modeling of 2008 Kasatochi volcanic sulfate direct radiative forcing: assimilation
1586 of OMI SO₂ plume height data and comparison with MODIS and CALIOP
1587 observations, *Atmos. Chem. Phys.*, 13, 1895-1912, 10.5194/acp-13-1895-2013,
1588 2013.

1589 Wang, L., Lyu, B., and Bai, Y.: Global aerosol vertical structure analysis by clustering
1590 gridded CALIOP aerosol profiles with fuzzy k-means, *Sci. Total Environ.*, 761,
1591 144076, 10.1016/j.scitotenv.2020.144076, 2021a.

1592 Wang, Q., Zhou, C., Zhuge, X. Y., Liu, C., Weng, F. Z., and Wang, M. H.: Retrieval of

1593 cloud properties from thermal infrared radiometry using convolutional neural
1594 network, *Remote Sens. Environ.*, 278, 10.1016/j.rse.2022.113079, 2022.

1595 Wang, Q. Q., Jacob, D. J., Spackman, J. R., Perring, A. E., Schwarz, J. P., Moteki, N.,
1596 Marais, E. A., Ge, C., Wang, J., and Barrett, S. R. H.: Global budget and radiative
1597 forcing of black carbon aerosol: Constraints from pole-to-pole (HIPPO)
1598 observations across the Pacific, *J. Geophys. Res.:Atmos.*, 119, 195-206,
1599 10.1002/2013jd020824, 2014.

1600 Wang, Y., Wang, J., Xu, X. G., Henze, D. K., Qu, Z., and Yang, K.: Inverse modeling
1601 of SO₂ and NO_x emissions over China using multisensor satellite data - Part 1:
1602 Formulation and sensitivity analysis, *Atmos. Chem. Phys.*, 20, 6631-6650,
1603 10.5194/acp-20-6631-2020, 2020a.

1604 Wang, Y., Wang, J., Zhou, M., Henze, D. K., Ge, C., and Wang, W.: Inverse modeling
1605 of SO₂ and NO_x emissions over China using multisensor satellite data - Part 2:
1606 Downscaling techniques for air quality analysis and forecasts, *Atmos. Chem. Phys.*,
1607 20, 6651-6670, 10.5194/acp-20-6651-2020, 2020b.

1608 Wang, Y., Bagya Ramesh, C., Giangrande, S. E., Fast, J., Gong, X., Zhang, J., Tolga
1609 Odabasi, A., Oliveira, M. V. B., Matthews, A., Mei, F., Shilling, J. E., Tomlinson,
1610 J., Wang, D., and Wang, J.: Examining the vertical heterogeneity of aerosols over
1611 the Southern Great Plains, *Atmos. Chem. Phys.*, 23, 15671-15691, 10.5194/acp-
1612 23-15671-2023, 2023.

1613 Wang, Y. L., Huang, R., Song, S. J., Huang, Z. Y., and Huang, G.: Not All Images are
1614 Worth 16x16 Words: Dynamic Transformers for Efficient Image Recognition, 35th
1615 Annual Conference on Neural Information Processing Systems (NeurIPS), null,
1616 ELECTR NETWORK, Dec 06-14 2021, WOS:000922928400032, 2021.

1617 Wei, J., Li, Z., Guo, J., Sun, L., Huang, W., Xue, W., Fan, T., and Cribb, M.: Satellite-
1618 Derived 1-km-Resolution PM₁ Concentrations from 2014 to 2018 across China,
1619 *Environ. Sci. Technol.*, 53, 13265-13274, 10.1021/acs.est.9b03258, 2019.

1620 Weinzierl, B., Ansmann, A., Prospero, J. M., Althausen, D., Benker, N., Chouza, F.,

1621 Dollner, M., Farrell, D., Fomba, W. K., Freudenthaler, V., Gasteiger, J., Gross, S.,
1622 Haarig, M., Heinold, B., Kandler, K., Kristensen, T. B., Mayol-Bracero, O. L.,
1623 Müller, T., Reitebuch, O., Sauer, D., Schäfler, A., Schepanski, K., Spanu, A., Tegen,
1624 I., Toledano, C., and Walser, A.: The Saharan Aerosol Long-Range Transport and
1625 Aerosol–Cloud-Interaction Experiment: Overview and Selected Highlights, *Bull.*
1626 *Am. Meteorol. Soc.*, 98, 1427-1451, 10.1175/bams-d-15-00142.1, 2017.

1627 Wilcox, E. M.: Direct and semi-direct radiative forcing of smoke aerosols over clouds,
1628 *Atmos. Chem. Phys.*, 12, 139-149, 10.5194/acp-12-139-2012, 2012.

1629 Winker, D. M., Tackett, J. L., Getzewich, B. J., Liu, Z., Vaughan, M. A., and Rogers, R.
1630 R.: The global 3-D distribution of tropospheric aerosols as characterized by
1631 CALIOP, *Atmos. Chem. Phys.*, 13, 3345-3361, 10.5194/acp-13-3345-2013, 2013.

1632 Winker, D. M., Vaughan, M. A., Omar, A., Hu, Y. X., Powell, K. A., Liu, Z. Y., Hunt,
1633 W. H., and Young, S. A.: Overview of the CALIPSO Mission and CALIOP Data
1634 Processing Algorithms, *J. Atmos. Oceanic Technol.*, 26, 2310-2323,
1635 10.1175/2009jtecha1281.1, 2009.

1636 Winker, D. M., Pelon, J., Coakley, J. A., Ackerman, S. A., Charlson, R. J., Colarco, P.
1637 R., Flamant, P., Fu, Q., Hoff, R. M., Kittaka, C., Kubar, T. L., Le Treut, H.,
1638 McCormick, M. P., Mégie, G., Poole, L., Powell, K., Trepte, C., Vaughan, M. A.,
1639 and Wielicki, B. A.: The CALIPSO Mission: A Global 3D View of Aerosols and
1640 Clouds, *Bull. Am. Meteorol. Soc.*, 91, 1211-1229, 10.1175/2010bams3009.1, 2010.

1641 Xing, J., Zheng, S. X., Li, S. W., Huang, L., Wang, X. C., Wang, S. X., Liu, C., Jang,
1642 C., Zhu, Y., Zhang, J., Bian, J., Liu, T. Y., Hao, J. M., and Kelly, J. T.: Mimicking
1643 atmospheric photochemical modeling with a deep neural network, *Atmos. Res.*,
1644 265, 10.1016/j.atmosres.2021.105919, 2022.

1645 Xiong, J., Wang, Y., Tao, M., Dong, W., Zhou, L., and Wang, L.: Vertical structure of
1646 the aerosols in the troposphere over the North China Plain: An analysis based on
1647 observations and simulations from 2007 to 2022, *Atmos. Res.*,
1648 10.1016/j.atmosres.2025.108348, 2025.

1649 Xu, Y., Ramanathan, V., and Washington, W. M.: Observed high-altitude warming and
1650 snow cover retreat over Tibet and the Himalayas enhanced by black carbon
1651 aerosols, *Atmos. Chem. Phys.*, 16, 1303-1315, 10.5194/acp-16-1303-2016, 2016.

1652 Yang, J., Zang, L., Mao, F., Zhang, Y., Xu, W., Liu, F., and Liu, T.: Optimizing MERRA-
1653 2 aerosol extinction coefficient by fusing CALIPSO and SAGE observations with
1654 machine learning, *Atmos. Environ.*, 363, 10.1016/j.atmosenv.2025.121619, 2025.

1655 Yorks, J. E., Wang, J., McGill, M. J., Follette-Cook, M., Nowotnick, E. P., Reid, J. S.,
1656 Colarco, P. R., Zhang, J., Kalashnikova, O., Yu, H., Marenco, F., Santanello, J. A.,
1657 Weckwerth, T. M., Li, Z., Campbell, J. R., Yang, P., Diao, M., Noel, V., Meyer, K.
1658 G., Carr, J. L., Garay, M., Christian, K., Bennedetti, A., Ring, A. M., Crawford, A.,
1659 Pavolonis, M. J., Aquila, V., Kim, J., and Kondragunta, S.: A SmallSat Concept to
1660 Resolve Diurnal and Vertical Variations of Aerosols, Clouds, and Boundary Layer
1661 Height, *Bull. Am. Meteorol. Soc.*, 104, E815-E836, 10.1175/bams-d-21-0179.1,
1662 2023.

1663 Zarzycki, C. M. and Bond, T. C.: How much can the vertical distribution of black carbon
1664 affect its global direct radiative forcing?, *Geophys. Res. Lett.*, 37,
1665 10.1029/2010gl044555, 2010.

1666 Zeng, Y., Wang, M., Zhao, C., Chen, S., Liu, Z., Huang, X., and Gao, Y.: WRF-Chem
1667 v3.9 simulations of the East Asian dust storm in May 2017: modeling sensitivities
1668 to dust emission and dry deposition schemes, *Geosci. Model Dev.s*, 13, 2125-2147,
1669 10.5194/gmd-13-2125-2020, 2020.

1670 Zhai, S. X., Jacob, D. J., Brewer, J. F., Li, K., Moch, J. M., Kim, J., Lee, S., Lim, H.,
1671 Lee, H. C., Kuk, S. K., Park, R. J., Jeong, J., Wang, X., Liu, P. F., Luo, G., Yu, F.
1672 Q., Meng, J., Martin, R., Travis, K. R., Hair, J. W., Anderson, B. E., Dibb, J. E.,
1673 Jimenez, J. L., Campuzano-Jost, P., Nault, B. A., Woo, J. H., Kim, Y., Zhang, Q.,
1674 and Liao, H.: Relating geostationary satellite measurements of aerosol optical
1675 depth (AOD) over East Asia to fine particulate matter (PM_{2.5}): insights from the
1676 KORUS-AQ aircraft campaign and GEOS-Chem model simulations, *Atmos.*

1677 Chem. Phys., 21, 16775-16791, 10.5194/acp-21-16775-2021, 2021.

1678 Zhang, J. L., Campbell, J. R., Reid, J. S., Westphal, D. L., Baker, N. L., Campbell, W.
1679 F., and Hyer, E. J.: Evaluating the impact of assimilating CALIOP-derived aerosol
1680 extinction profiles on a global mass transport model, *Geophys. Res. Lett.*, 38,
1681 10.1029/2011gl047737, 2011.

1682 Zhao, B., Wang, Y., Gu, Y., Liou, K.-N., Jiang, J. H., Fan, J., Liu, X., Huang, L., and
1683 Yung, Y. L.: Ice nucleation by aerosols from anthropogenic pollution, *Nat. Geosci.*,
1684 12, 602-607, 10.1038/s41561-019-0389-4, 2019.

1685 Zhen, Y., Yang, X., Tang, H., Shi, H., and Liu, Z.: CALIPSO-based aerosol extinction
1686 profile estimation from MODIS and MERRA-2 data using a hybrid model of
1687 Transformer and CNN, *Sci. Total Environ.*, 954, 10.1016/j.scitotenv.2024.176423,
1688 2024.

1689 Zhu, H. H., Martin, R. V., van Donkelaar, A., Hammer, M. S., Li, C., Meng, J., Oxford,
1690 C. R., Liu, X., Li, Y. S., Zhang, D. D., Singh, I., and Lyapustin, A.: Importance of
1691 aerosol composition and aerosol vertical profiles in global spatial variation in the
1692 relationship between PM_{2.5} and aerosol optical depth, *Atmos. Chem. Phys.*, 24,
1693 11565-11584, 10.5194/acp-24-11565-2024, 2024.

1694

1695 Table 1. Experimental design based on the Leave-One-Year-Out cross-validation
1696 strategy.

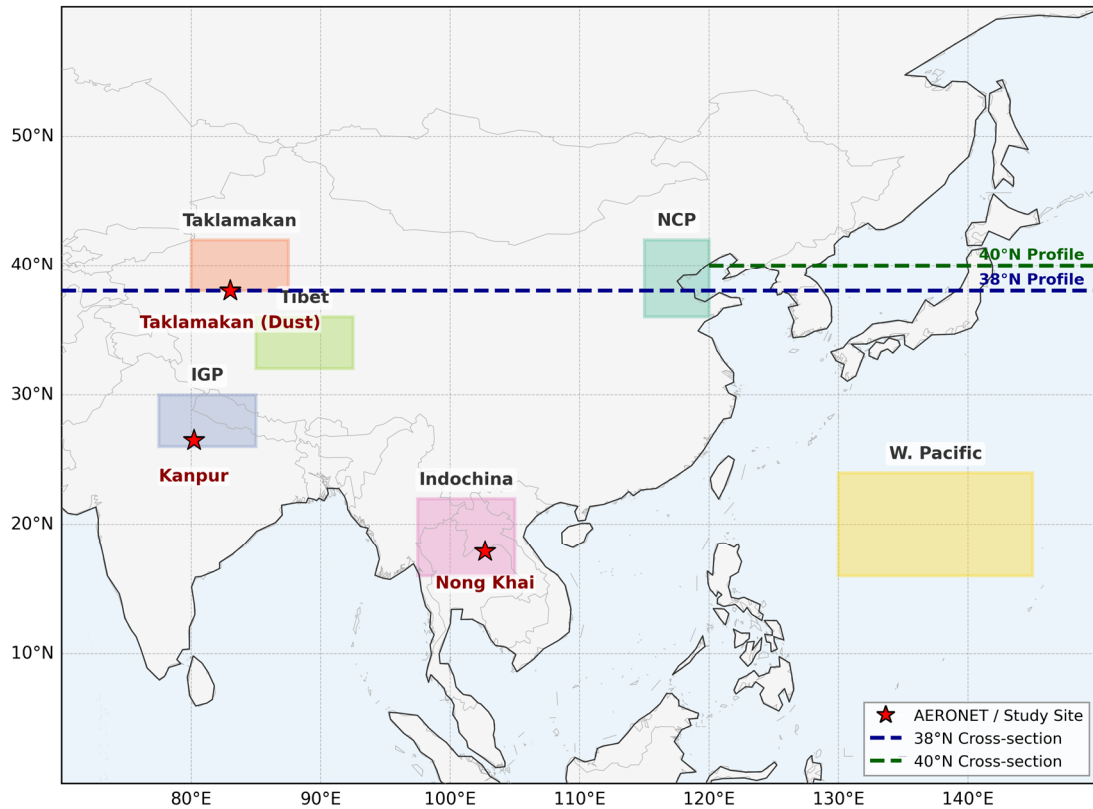
Experiment ID	Training & Validation Data	Test Data	Evaluation Objective
Exp-2017	Years 2018, 2019	Year 2017	Hindcasting
Exp-2018	Years 2017, 2019	Year 2018	Temporal Interpolation
Exp-2019	Years 2017, 2018	Year 2019	Forecasting

1697

1698 Table 2. Quantitative evaluation of the physics-informed Transformer model's
1699 predictive performance for AEC simulation biases over EA across independent test
1700 years based on the Leave-One-Year-Out strategy.

Experiment ID	R	MAE (km ⁻¹)	RMSE (km ⁻¹)
Exp-2017	0.666	0.014	0.039
Exp-2018	0.659	0.014	0.039
Exp-2019	0.651	0.015	0.041
Average	0.659	0.014	0.040

1701



1702

1703 Figure 1. Map of the study domain covering East and South Asia (0°-60°N, 70°-150°E).

1704 The colored rectangles delimitate the six ROI selected for regional analysis. The dashed

1705 lines represent the latitudinal transects at 38°N (blue) and 40°N (green) used for vertical

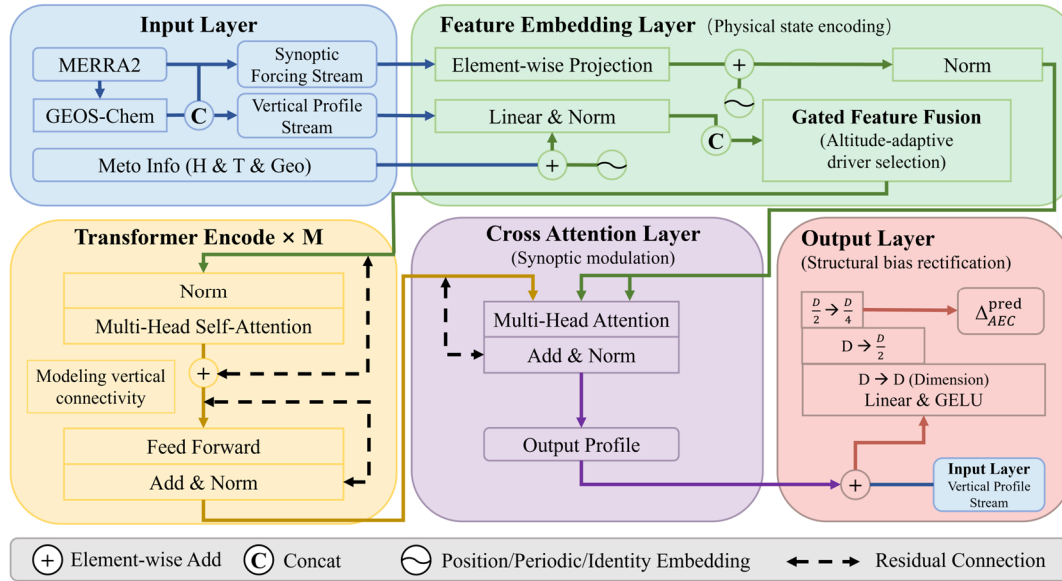
1706 profile cross-section analysis. Red stars indicate the specific study sites selected to

1707 represent distinct aerosol regimes: the Kanpur and Nong Khai sites are AERONET

1708 ground-based stations selected to represent regions dominated by anthropogenic

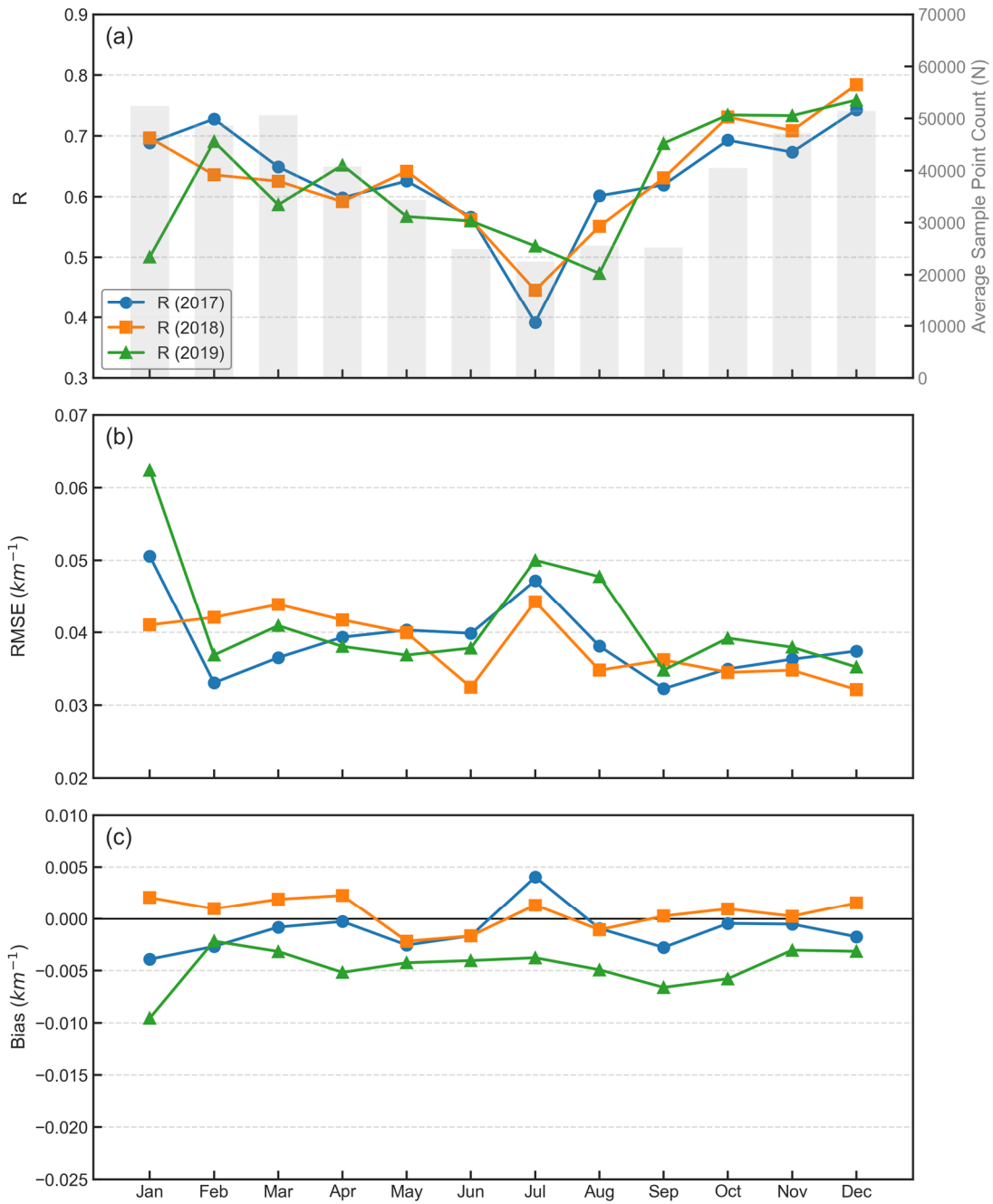
1709 pollution and biomass burning, respectively; the Taklamakan site marks a reference

1710 location selected to investigate the characteristics of natural mineral dust.



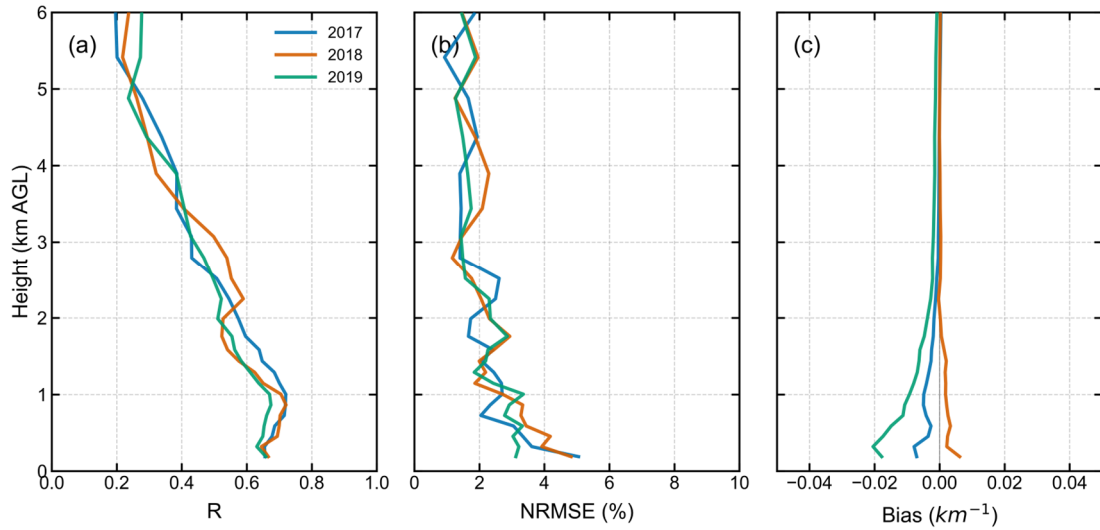
1711

1712 Figure 2. Architecture of the physics-informed Transformer framework. The Feature
 1713 Embedding Layer integrates the VPS and SFS into unified, high-dimensional physical
 1714 states. Gated Feature Fusion resolves atmospheric stratification by dynamically
 1715 prioritizing altitude-dependent drivers. The Transformer Encoder stack models vertical
 1716 connectivity, simulating exchange processes like turbulent mixing to ensure profile
 1717 coherence. The Cross-Attention Layer retrieval synoptic constraints to modulate AEC
 1718 corrections based on the meteorological background. The Output Layer performs
 1719 residual bias rectification, anchoring the prediction to the initial physicochemical
 1720 profiles to accurately quantify systematic simulation biases while filtering redundant
 1721 noise.



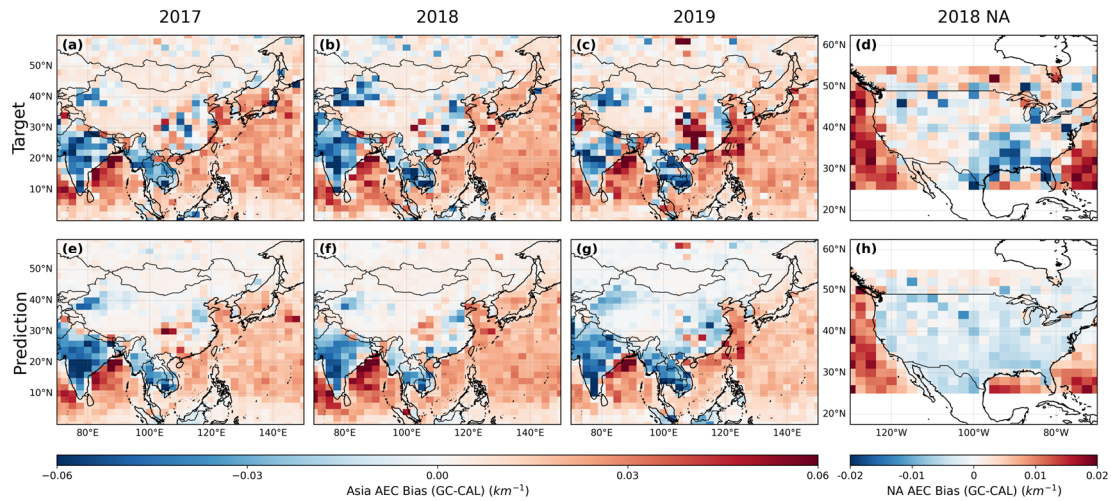
1722

1723 Figure 3. Monthly variations of statistical metrics evaluating the physics-informed
 1724 Transformer model's predictive performance over EA across the three test years (2017,
 1725 2018, and 2019). The panels display the time series of R between the AEC bias
 1726 predicted by the model and that simulated by GEOS-Chem (a), along with the multi-
 1727 year average monthly sample size (N, gray bars), RMSE (b), and mean bias (c).



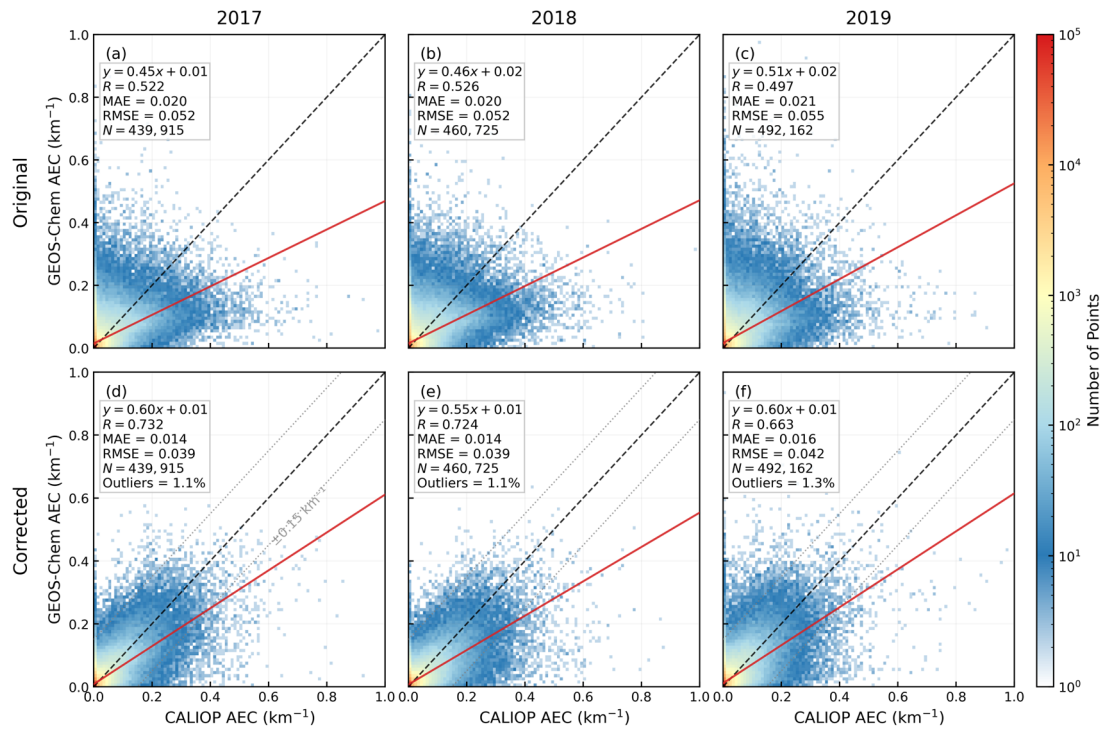
1728

1729 Figure 4. Vertical profiles of the physics-informed Transformer model's predictive
 1730 performance for AEC simulation bias over EA across three independent test years (2017,
 1731 2018, and 2019). The panels show the height-resolved R (a), NRMSE (b), and mean
 1732 bias (c). The performance is evaluated against CALIOP observations from the surface
 1733 up to 6 km AGL.



1734

1735 Figure 5. Spatial comparison of the vertically averaged (0–6 km AGL) AEC simulation
 1736 bias over EA and NA. The top row (a–d) represents the Target systematic bias. The
 1737 bottom row (e–h) displays the corresponding bias predicted by the physics-informed
 1738 Transformer model. Columns 1–3 show results for the independent test years (2017,
 1739 2018, 2019) over the primary EA domain (a–c, e–g). Column 4 presents the
 1740 generalization test over the NA domain for 2018 (d, h), where the model trained on EA
 1741 data is directly applied to predict biases in an unseen continent.



1742

1743 Figure 6. Density scatter plots comparing the simulated AEC against CALIOP

1744 observations over EA for the three test years: 2017 (a, d), 2018 (b, e), and 2019 (c, f).

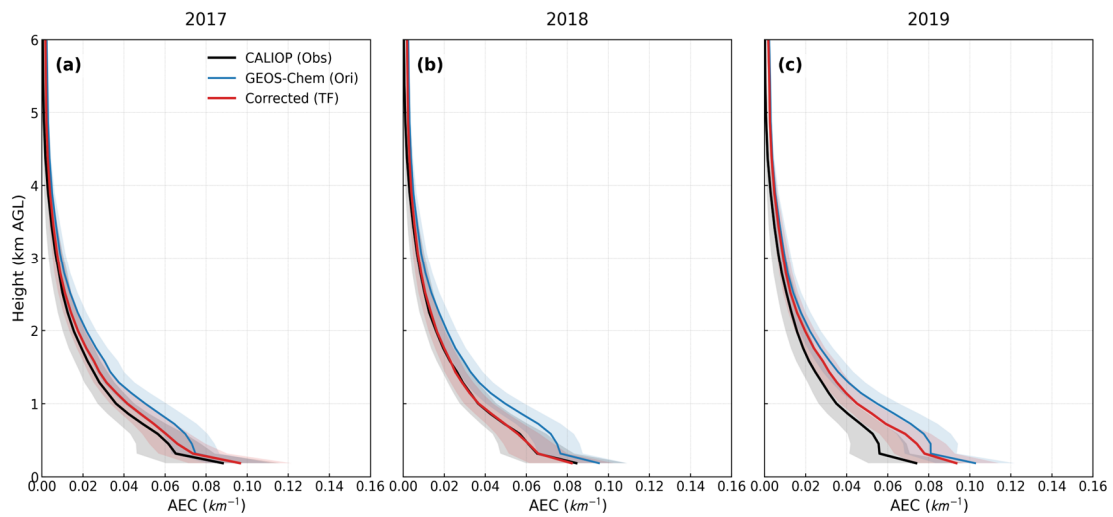
1745 The top row (a, b, c) displays the validation results for the original GEOS-Chem

1746 simulation, while the bottom row (d, e, f) shows the results after correction by the

1747 physics-informed Transformer model. The dashed gray lines in the bottom panels (d–f)

1748 delineate the $\pm 0.15 \text{ km}^{-1}$ error envelope, with the corresponding percentage of outliers

1749 (points falling outside this envelope) indicated in the statistical boxes.



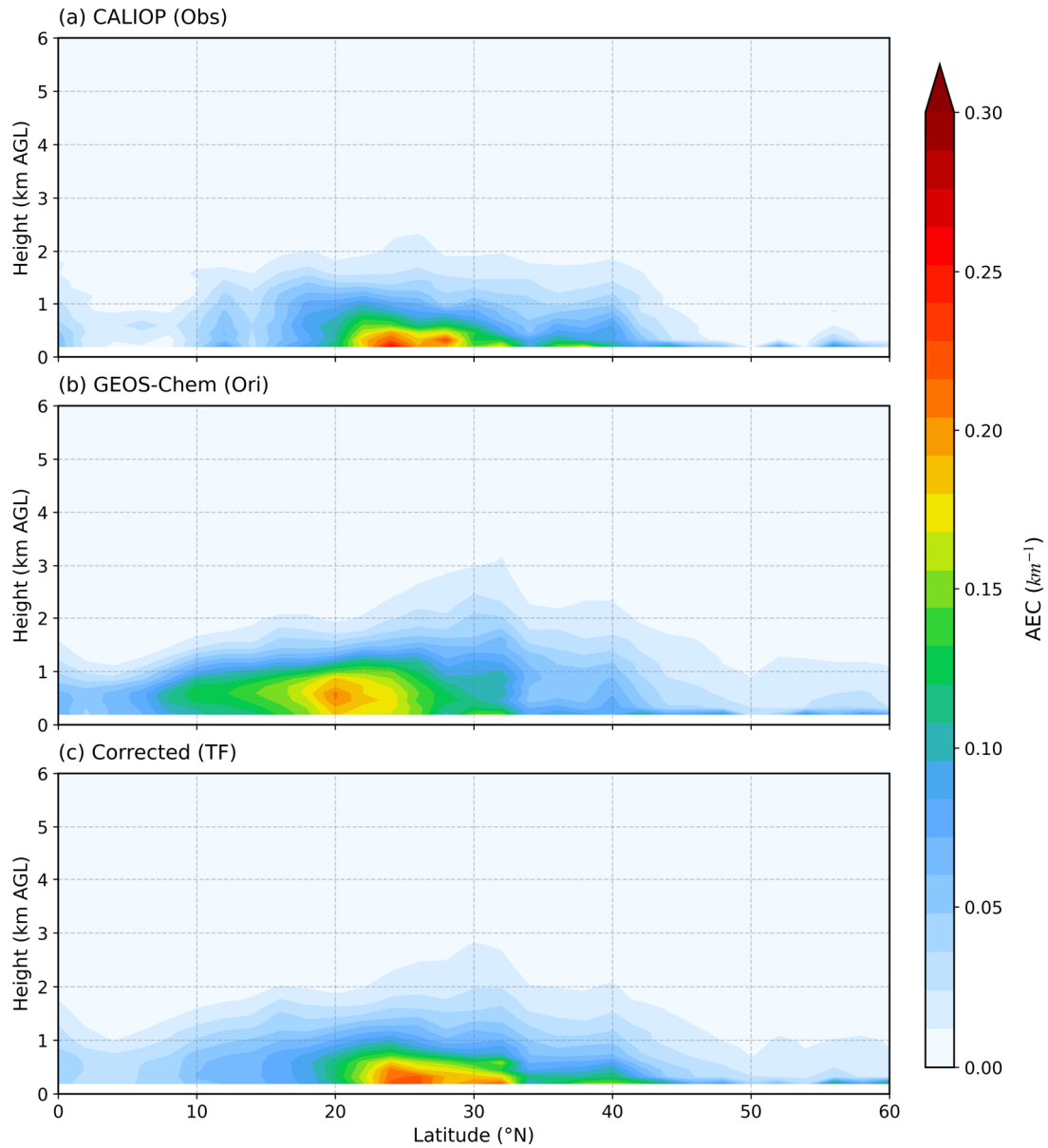
1750

1751 Figure 7. Annual mean vertical profiles of AEC for the three test years (2017–2019).

1752 The profiles are averaged over the entire study domain (EA). The shaded areas indicate

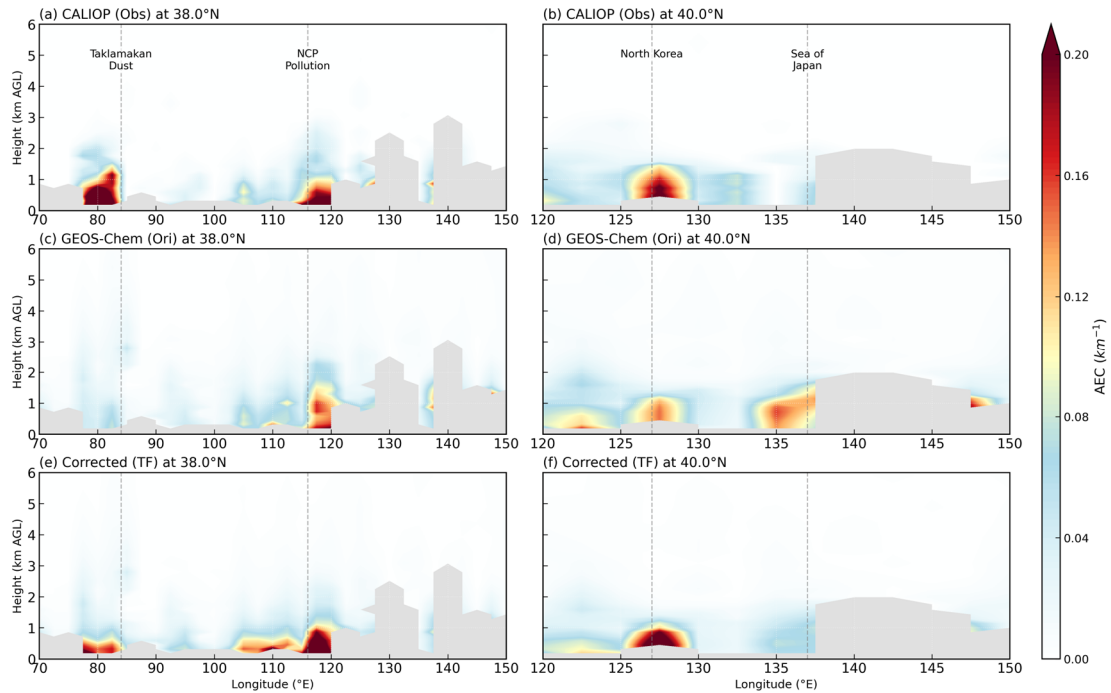
1753 the standard deviation ($\pm 0.5\sigma$) of the vertical distribution, representing the spatial and

1754 temporal variability.



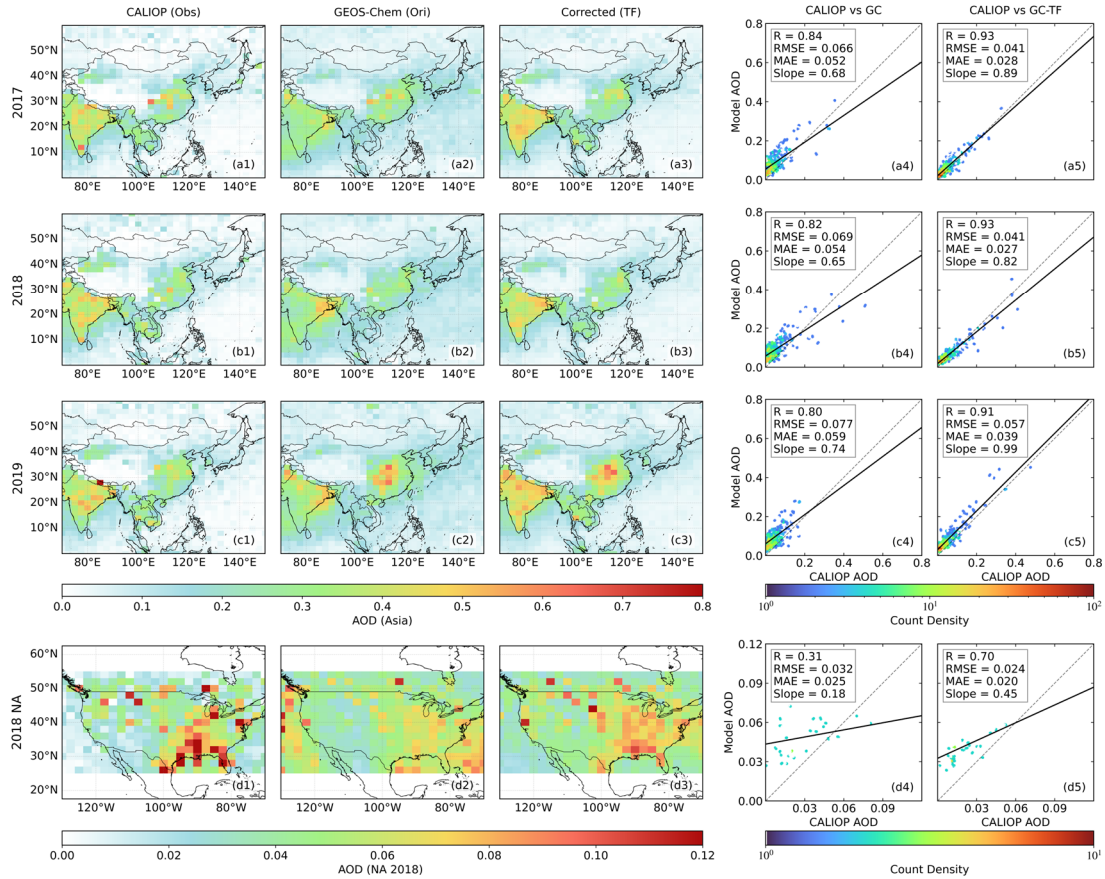
1755

1756 Figure 8. Zonal mean vertical distributions of AEC averaged over the longitude range
 1757 (70°E–150°E) for the test year 2019. The panels display the latitude-altitude cross-
 1758 sections for CALIOP observations (a), original GEOS-Chem simulations (b), and the
 1759 corrected GC-TF results (c).



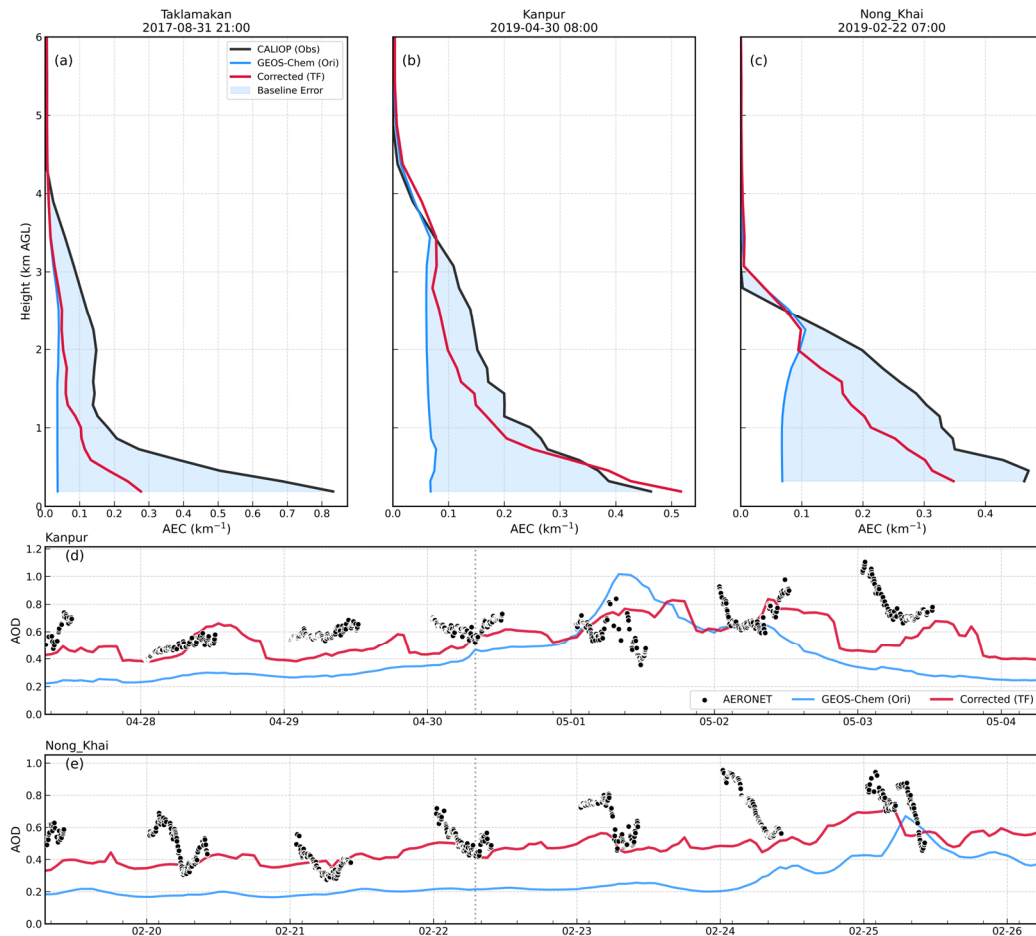
1760

1761 Figure 9. Longitudinal vertical cross-sections of annual mean AEC along two selected
 1762 latitudes for the test year 2019. The left column displays the profiles at 38.0°N,
 1763 highlighting the Taklamakan Desert and the NCP. The right column displays the profiles
 1764 at 40.0°N, capturing the aerosol transport over the Korean Peninsula and the Sea of
 1765 Japan. Panels show CALIOP observations (a, b), original GEOS-Chem simulations (c,
 1766 d), and the corrected GC-TF results (e, f). The vertical dashed lines mark the
 1767 approximate locations of key geographical features. Gray areas indicate missing data.



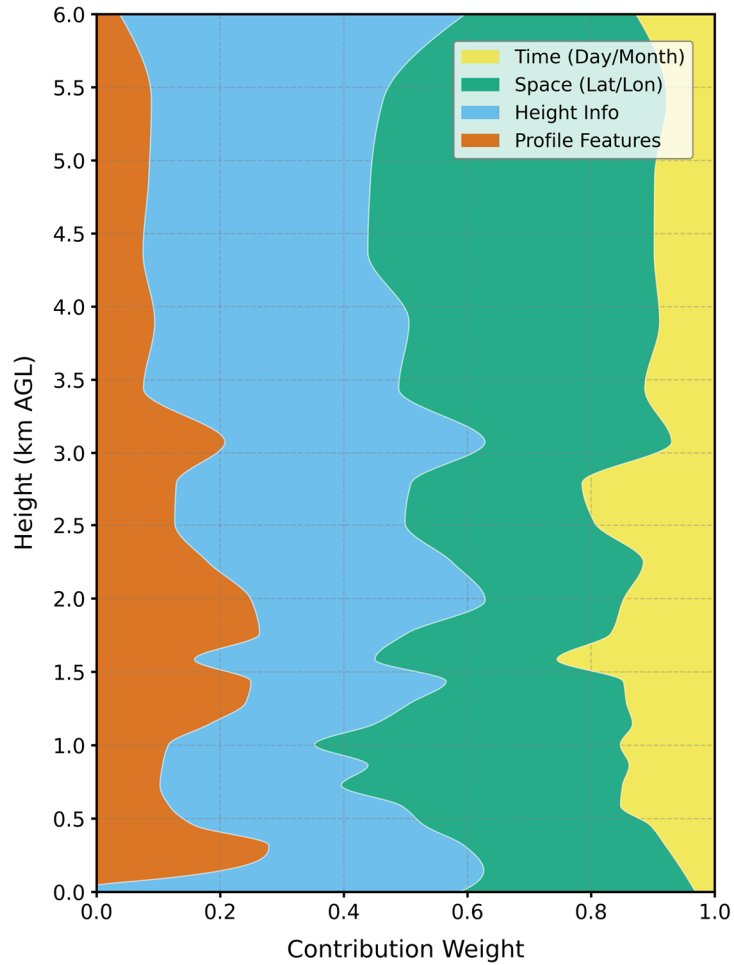
1768

1769 Figure 10. Spatial distributions and statistical evaluations of the annual mean AOD
 1770 derived from CALIOP observations, GEOS-Chem simulations, and the GC-TF model
 1771 corrections. Results for the EA domain during the test years 2017 (a), 2018 (b), and
 1772 2019 (c), respectively. Columns 1–3 display the spatial patterns of AOD from CALIOP,
 1773 the original GEOS-Chem (Ori), and the corrected GC-TF results (TF). Columns 4–5
 1774 show the corresponding density scatter plots comparing the model predictions (y-axis)
 1775 against CALIOP observations (x-axis). Generalization test over the NA domain for the
 1776 year 2018 (d).



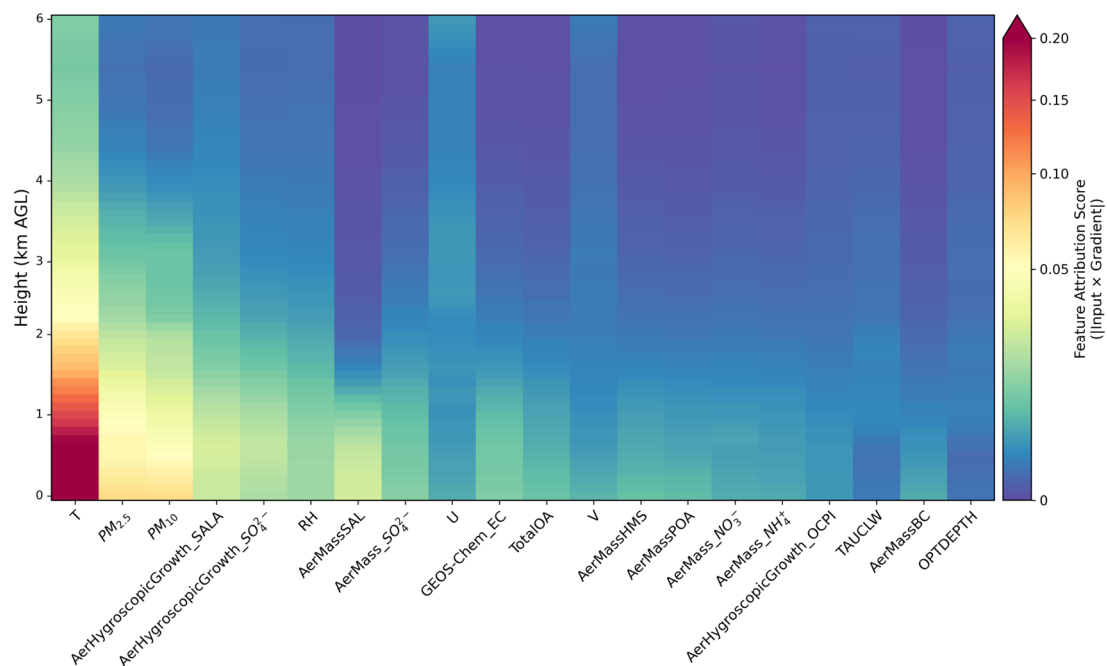
1777

1778 Figure 11. Composite analysis of aerosol vertical structures and temporal evolution
 1779 during selected pollution episodes. Vertical profiles of AEC at three representative sites:
 1780 Taklamakan (Dust, a), Kanpur (Anthropogenic Pollution, b), and Nong Khai (Biomass
 1781 Burning, c). Time series of AOD at the Kanpur (d) and Nong Khai (e) AERONET sites
 1782 during the corresponding pollution events. The vertical dotted lines mark the CALIOP
 1783 overpass times (UTC) shown in the top panels.



1784

1785 Figure 12. Altitude-dependent prioritization of information within the VPS. The stacked
 1786 plot displays the learnable contribution weights for the four VPS sub-components—
 1787 baseline physicochemical profiles, height information, spatial coordinates, and
 1788 temporal indices—as determined by the gated feature fusion mechanism. This analysis
 1789 visualizes how the model’s internal decision-making adapts to different atmospheric
 1790 stratifications.



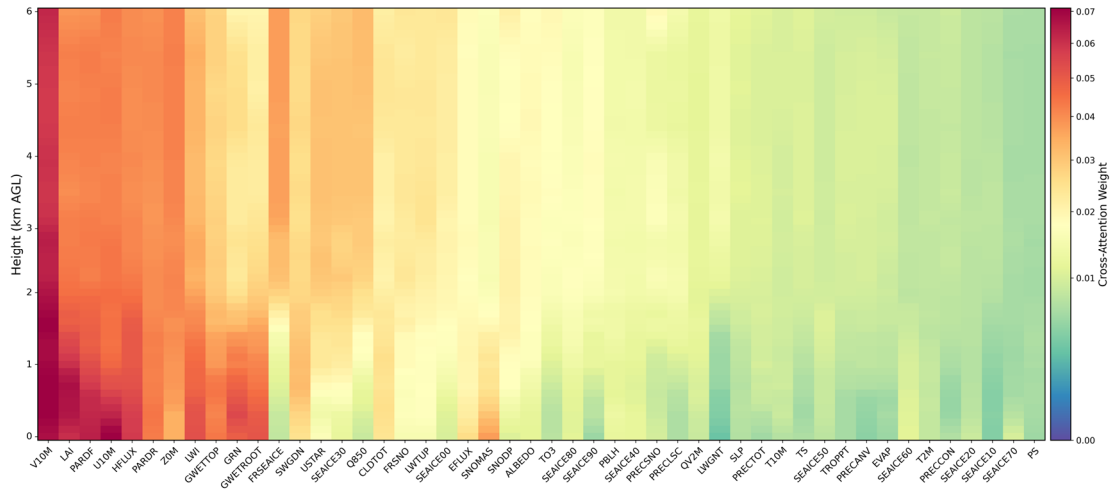
1791

1792 Figure 13. Vertical distribution of cross-attention weights for synoptic forcing variables.

1793 The heatmap characterizes the interaction strength between the SFS and the VPS. It

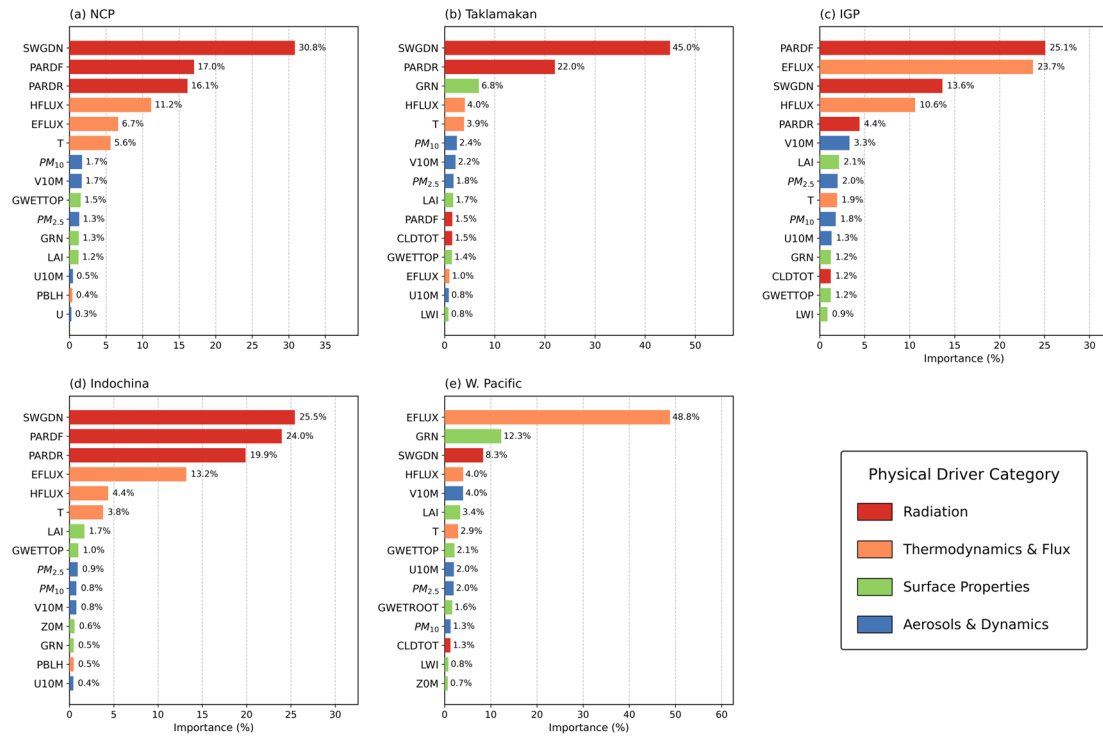
1794 reveals how specific variables within the SFS (sorted by total contribution from left to

1795 right) modulate AEC bias corrections at different altitude levels.



1796

1797 Figure 14. Vertical distribution of the attention weights for global variables learned by
 1798 the Cross-Attention module. The heatmap displays the interaction strength between the
 1799 VPS and the SFS. The variables are sorted by their total contribution from left to right.



1800

1801 Figure 15. Regional variability in feature importance drivers identified by SHAP
 1802 analysis for the test year 2019. The panels display the top 15 most influential features
 1803 for predicting AEC simulation biases in five representative regions: NCP (a),
 1804 Taklamakan Desert (b), IGP (c), Indochina (d), and Western Pacific (e).